bioRxiv preprint doi: https://doi.org/10.1101/696195; this version posted July 8, 2019. The copyright holder for this preprint (which was not certified by peer review) is the author/funder, who has granted bioRxiv a license to display the preprint in perpetuity. It is made available under aCC-BY 4.0 International license.

Within-host dynamics of virulent viruses in bat reservoirs for emerging zoonotic disease

Cara E. Brook[1,2†], Mike Boots[1], Kartik Chandran[3], Andrew P. Dobson[2], Christian Drosten[4], Andrea L. Graham[2], Bryan T. Grenfell[2,5], Marcel A. Müller[4,6], Melinda Ng[3], Lin-Fa Wang[7], Anieke van Leeuwen[2,8]

[1] Department of Integrative Biology, University of California, Berkeley, Berkeley, CA, USA.

[2] Department of Ecology & Evolutionary Biology, Princeton University, Princeton, NJ, USA.

[3] Department of Microbiology and Immunology, Albert Einstein College of Medicine, Bronx, NY, USA.

[4] Institute of Virology, Charité Universitätsmedizin, Berlin, Germany.

[5] Fogarty International Center, National Institutes of Health, Bethesda, Maryland, USA.

[6] Martsinovsky Institute of Medical Parasitology, Tropical and Vector Borne Diseases, Sechenov University, Moscow, Russia.

[7] Emerging Infectious Diseases Program, Duke-National University of Singapore Medical School, Singapore.

[8] Royal Netherlands Institute for Sea Research, Department of Coastal Systems, and Utrecht University, the Netherlands

bioRxiv preprint doi: https://doi.org/10.1101/696195; this version posted July 8, 2019. The copyright holder for this preprint (which was not certified by peer review) is the author/funder, who has granted bioRxiv a license to display the preprint in perpetuity. It is made available under aCC-BY 4.0 International license.

Abstract

Understanding the factors underpinning emergence and reemergence of virulent viral zoonoses is of critical importance. In particular, bats are known to host virulent zoonotic viruses without experiencing disease. Previous work suggests that bats' viral hosting capacities may partially result from uniquely constitutive immune capabilities, but the impact of these defenses on viral dynamics within-host has yet to be explored. We carried out viral infectivity assays on bat cell lines expressing induced and constitutive immune phenotypes, then developed a theoretical model of our *in vitro* system, which we fit to empirical data to estimate rates of within-host viral propagation and assumption of antiviral defenses. Persistent viral infections established under both induced and constitutive immune assumptions, but constitutive immunity produced consistently faster within-host viral propagation rates. Faster-replicating viruses evolved in bat hosts possessing perpetually antiviral immune capabilities are likely to exhibit enhanced virulence following emergence into novel hosts lacking constitutive immunity.

bioRxiv preprint doi: https://doi.org/10.1101/696195; this version posted July 8, 2019. The copyright holder for this preprint (which was not certified by peer review) is the author/funder, who has granted bioRxiv a license to display the preprint in perpetuity. It is made available under aCC-BY 4.0 International license.

Introduction

Bats have received much attention in recent years for their role as reservoir hosts for emerging viral zoonoses, including rabies lyssavirus, Hendra and Nipah henipaviruses, Ebola and Marburg filoviruses, and SARS coronavirus (Calisher, Childs, Field, Holmes, & Schountz, 2006; Wang & Anderson, 2019). In non-Chiropteran mammals, henipaviruses, filoviruses, and coronaviruses induce substantial morbidity and mortality, display short durations of infection, and elicit robust, long-term immunity in hosts surviving infection (Hooper, Zaki, Daniels, & Middleton, 2001; Mahanty & Bray, 2004; Nicholls et al., 2003). Bats, by contrast, demonstrate no obvious disease symptoms upon infection with pathogens virulent in non-volant mammals (Schountz, 2014) and may support viruses as long-term persistent infections, rather than transient, immunizing pathologies (Plowright et al., 2016). Recent molecular work highlights unique bat adaptations to combat inflammation (Ahn et al., 2019; Pavlovich et al., 2018; Xie et al., 2018; Zhang et al., 2013), thought to have evolved to mitigate metabolic damage induced during flight (Kacprzyk et al., 2017), which may safeguard bats against the immunopathology (i.e. hemorrhagic fever) that bat-associated viruses typically elicit in other mammals (Brook & Dobson, 2015).

In addition to mitigating immunopathology, bats also manage health by limiting viral infection through species-specific, resistance mechanisms. One recently-described amino acid substitution in the filovirus receptor, Niemann-Pick C1 (NPC1), renders cells of the African straw-colored fruit bat, *Eidolon helvum*, refractory to infection with Ebola (Ng et al., 2015). Constitutive expression of the antiviral cytokine, IFN-α, has furthermore been demonstrated in two other fruit bat species (Zhou et al., 2016). The extent to which this latter defense is truly constitutive, versus induced upon viral exposure, remains unresolved. By definition, an effective

bioRxiv preprint doi: https://doi.org/10.1101/696195; this version posted July 8, 2019. The copyright holder for this preprint (which was not certified by peer review) is the author/funder, who has granted bioRxiv a license to display the preprint in perpetuity. It is made available under aCC-BY 4.0 International license.

reservoir host will need to permit some pathogen invasion and replication (Haydon, Cleaveland, Taylor, & Laurenson, 2002), thus constraining the range of constitutive defenses permissible in the bat-virus system broadly. We investigated the impact of induced versus constitutive immunity on bat viral dynamics within-host using an innovative combination of cell culture experimentation and modeling tools.

Typically, the presence of viral RNA or DNA in the cytoplasm of mammalian cells will induce secretion of type I interferon proteins (IFN-α and IFN-β), which promote expression and translation of interferon-stimulated genes (ISGs) in neighboring cells and render them effectively antiviral (Stetson & Medzhitov, 2006). The extent to which constitutive IFN-α expression signifies constitutive antiviral defense versus primed, inducible defense remains unresolved; in nature, immune pathways are so complex that perfect constitutive immunity is unlikely for any given bat-virus interaction. In bat cells constitutively expressing IFN-α, some ISGs appear to be also constitutively expressed (suggestive of functional IFN-α protein in the system), but additional ISG induction is nonetheless possible following viral challenge and stimulation of IFN-β (Zhou et al., 2016).

To investigate the impact of induced versus constitutive antiviral defenses on viral kinetics, we first undertook a series of viral infection experiments on bat cell lines expressing divergent interferon phenotypes, then developed and analyzed a theoretical model, elucidating the dynamics of within-host viral spread under diverse assumptions of immunity. We fit this model to data recovered from our *in vitro* experimental trials to estimate rates of viral transmission and cellular progression to antiviral status. Finally, we constructed a spatially-structured individual-based extension of our initial mean field ('well-mixed') model, which we also fit to experimental data, and used to simulate the probability of pathogen persistence versus

bioRxiv preprint doi: https://doi.org/10.1101/696195; this version posted July 8, 2019. The copyright holder for this preprint (which was not certified by peer review) is the author/funder, who has granted bioRxiv a license to display the preprint in perpetuity. It is made available under aCC-BY 4.0 International license.

stochastic extinction under varying antiviral immune strategies. We hypothesized that constitutive immune processes would favor pathogen extinction, while robust induced defenses would best support viral persistence by permitting initial viral invasion but enabling rapid suppression of viral replication to low levels.

Results

Viral propagation is dampened in constitutively antiviral cell cultures.

We first explored the influence of innate immune phenotype on within-host viral propagation in a series of infection experiments in cell culture. We conducted plaque assays on six-well plate monolayers of three immortalized mammalian kidney cell lines: [1] Vero (African green monkey) cells, which are IFN-defective and thus limited in antiviral capacity (Desmyter, Melnick, & Rawls, 1968); [2] RoNi/7.1 (*Rousettus aegyptiacus*) cells which demonstrate idiosyncratic induced interferon responses upon viral challenge (Arnold et al., 2018; Biesold et al., 2011; Kuzmin et al., 2017; Omatsu et al., 2008; Pavlovich et al., 2018); and [3] PaKiT01 (*Pteropus alecto*) cells which constitutively express IFN-α (Crameri et al., 2009; Zhou et al., 2016). To intensify cell line-specific differences in constitutive immunity, we carried out infectivity assays with GFP-tagged, replication-competent vesicular stomatitis Indiana viruses: rVSV-G, rVSV-EBOV, and rVSV-MARV, which have been previously described (Miller et al., 2012; Wong, Sandesara, Mulherkar, Whelan, & Chandran, 2010). Previous work in this lab has demonstrated incompatibilities in the NPC1 filovirus receptor which render PaKiT01 cells refractory to infection with rVSV-MARV (Ng & Chandran, 2018), making them structurally antiviral, over and above their constitutive expression of IFN-α. All three cell lines were challenged with all three viruses at two multiplicities of infection (MOI): 0.001 and 0.0001.

bioRxiv preprint doi: https://doi.org/10.1101/696195; this version posted July 8, 2019. The copyright holder for this preprint (which was not certified by peer review) is the author/funder, who has granted bioRxiv a license to display the preprint in perpetuity. It is made available under aCC-BY 4.0 International license.

Because plaque assays restrict viral transmission neighbor-to-neighbor in two-dimensional cellular space (Howat, Barreca, O'Hare, Gog, & Grenfell, 2006), we were able to track the spread of GFP-expressing virally-infected cells across tissue monolayers using an inverted fluorescence microscope. For each infection trial, we monitored and re-imaged plates for up to 200 hours of observations or until total monolayer destruction, processed resulting images, and generated a time series of the proportion of infectious-cell occupied plate space across the duration of each trial (see Methods). We then used generalized additive models to determine the statistical mean of each cell line-virus-MOI specific experiment and generate the empirical data to which we eventually fit our mechanistic transmission models (Figure 1).

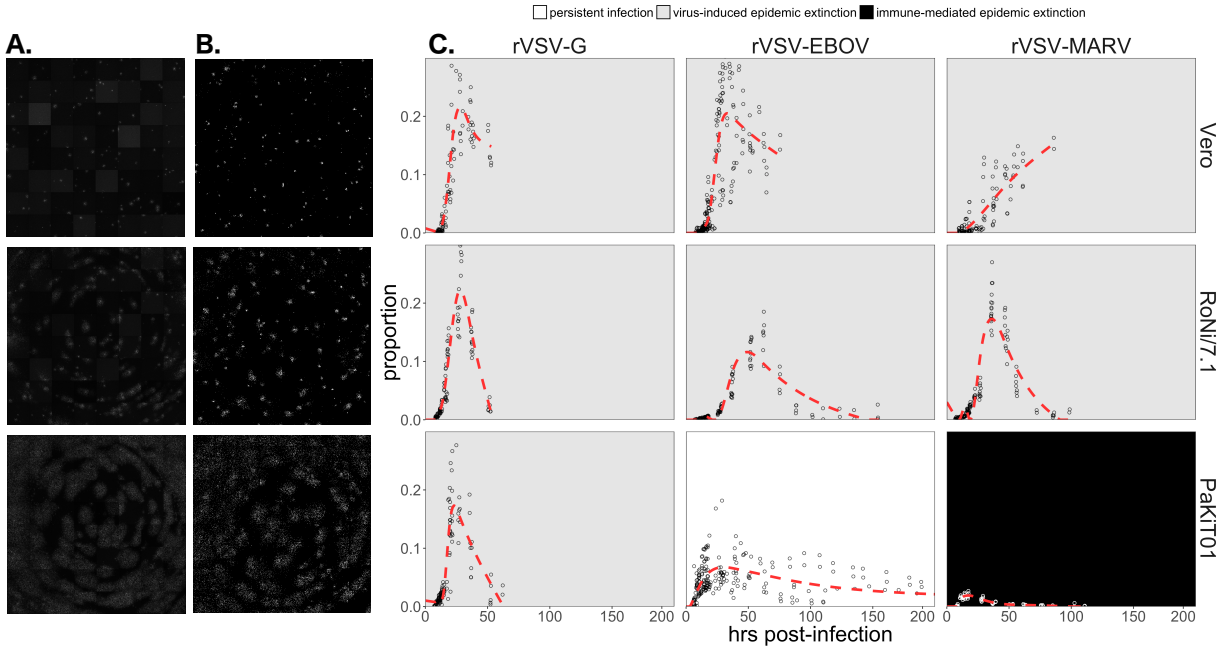

Figure 1. Cell culture models of viral propagation. Column (A) shows raw, original images of rVSV-EBOV propagation across Vero cell lines at, respectively, 17, 21, and 28 hours post-infection (timesteps 2, 3, and 5 from trial Ver6_B1). Column (B) lists corresponding, binary images processed in the R package, EBImage. Cells expressing viral eGFP are depicted in white and uninfected/dead cells in black. Block (C) shows raw time series data from quantification of binary images for rVSV-G, rVSV-EBOV, and rVSV-MARV infections (columns) on Vero, RoNi/7.1, and PaKiT01 cell lines (rows) at MOI=0.001. Open circles show raw data across all trials, while the red, dashed line gives the statistical mean across these trials, established from

bioRxiv preprint doi: https://doi.org/10.1101/696195; this version posted July 8, 2019. The copyright holder for this preprint (which was not certified by peer review) is the author/funder, who has granted bioRxiv a license to display the preprint in perpetuity. It is made available under aCC-BY 4.0 International license.

GAM model incorporating random effects per trial. Panel background shading corresponds to the mean result of all experimental trials for each cell line–virus combination (persistent infection = white; virus-induced epidemic extinction = gray; immune-mediated epidemic extinction = black). Raw data for MOI=0.0001 trials are available in SI Appendix, Figure S1.

All three recombinant vesicular stomatitis viruses (rVSV-G, rVSV-EBOV, and rVSV-MARV) infected Vero, RoNi/7.1, and PaKiT01 tissue cultures at both focal MOIs. Post-invasion, virus spread rapidly across most cell monolayers, resulting in epidemic decline and virus-induced epidemic extinction. Two exceptions to this general pattern occurred in the case of rVSV-EBOV and rVSV-MARV infections on PaKiT01 cells: in the former, persistent viral infection was maintained throughout the 200-hour duration of each experiment, while, in the latter, infection was eliminated early in the time series, preserving a large proportion of live, uninfectious cells across the duration of the experiment. We assumed this pattern to be the result of immune-mediated epidemic extinction (Figure 1). Patterns from MOI=0.001 were largely recapitulated at MOI = 0.0001, though at somewhat reduced total proportions (SI Appendix, Fig S1).

A theoretical model for within-host viral dynamics.

We next developed and analyzed a theoretical within-host model to explore the effects of induced and constitutive immunity on the dynamics of viral spread in host tissue. Broadly, we aimed to expand our understanding of the dynamic dependencies in the system, and more specifically, we sought to fit this model to the time series data recovered from *in vitro* experiments outlined above in order to estimate critical parameters in the infectious process. Models of simple target cell depletion, without explicit consideration of top-down immune control, were first developed to describe fundamental within-host dynamics of HIV (Alan S. Perelson, 2002) and other chronic infections, including hepatitis-C virus (Neumann et al., 1998),

bioRxiv preprint doi: https://doi.org/10.1101/696195; this version posted July 8, 2019. The copyright holder for this preprint (which was not certified by peer review) is the author/funder, who has granted bioRxiv a license to display the preprint in perpetuity. It is made available under aCC-BY 4.0 International license.

hepatitis-B virus (Nowak et al., 1996), and cytomegalovirus (Emery, Cope, Bowen, Gor, & Griffiths, 1999). Recent work has applied similar techniques to acute infections, such as influenza A and measles, inspiring debate over the extent to which explicit modeling of top-down immune control can improve inference beyond the basic resource limitation assumptions of the target cell model (Baccam, Beauchemin, Macken, Hayden, & Perelson, 2006; Morris et al., 2018; Pawelek et al., 2012; Saenz et al., 2010). One spatially-structured model elucidating interferon-mediated suppression of herpes simplex virus-1 replication in bovine kidney cells *in vitro* inspired some of the assumptions we describe here (Howat et al., 2006).

The compartmental within-host system mimics our two-dimensional cell culture monolayer, with cells occupying five distinct infection states: susceptible (S), antiviral (A), exposed (E), infectious (I), and dead (D). We modeled exposed cells as infected but not yet infectious, capturing the 'eclipse phase' of viral integration into a host cell which precedes viral replication. Antiviral cells were immune to viral infection, in accordance with the "antiviral state" induced from interferon stimulation of ISGs in tissues adjacent to infection (Stetson & Medzhitov, 2006). Because we aimed to translate available data into modeled processes, we did not explicitly model interferon dynamics but instead scaled the rate of cell progression from susceptible to antiviral (ρ) by the proportion of exposed cells (globally) in the system. In systems permitting constitutive immunity, this rate additionally scaled with the proportion of susceptible cells in the model. Compared with virus, IFN particles are small and highly diffusive, thus easily justifying the global signaling assumption at the limited spatial extent of a six well plate and in accordance with previous modeling approximations of plaque assays (Howat et al., 2006).

To maintain consistency with our empirical monolayer system, we expressed our state variables as proportions (P_S, P_A, P_E, P_I, and P_D), under assumptions of frequency-dependent

bioRxiv preprint doi: https://doi.org/10.1101/696195; this version posted July 8, 2019. The copyright holder for this preprint (which was not certified by peer review) is the author/funder, who has granted bioRxiv a license to display the preprint in perpetuity. It is made available under aCC-BY 4.0 International license.

transmission in a well-mixed population (Keeling & Rohani, 2008), yielding the following system of ordinary differential equations:

$$\frac{dP_S}{dt} = bP_D P_S - \beta P_S P_I - \mu P_S - \rho(P_E P_S + \varepsilon P_S) + cP_A \quad (1)$$

$$\frac{dP_A}{dt} = \rho(P_E P_S + \varepsilon P_S) - cP_A - \mu P_A \quad (2)$$

$$\frac{dP_E}{dt} = \beta P_S P_I - \sigma P_E - \mu P_E \quad (3)$$

$$\frac{dP_I}{dt} = \sigma P_E - \alpha P_I - \mu P_I \quad (4)$$

$$\frac{dP_D}{dt} = \mu(P_S + P_E + P_I + P_A) + \alpha P_I - bP_D P_S \quad (5)$$

where b is the per capita cell birth rate, μ the natural mortality rate, σ the cellular incubation rate (inverse of the duration of the viral eclipse phase), and α the elevated rate of virus-induced mortality for infected cells. The transmission rate from susceptible to exposed is represented by β and scales with the proportion of infectious cells in the system. The progression rate of susceptible cells to antiviral status is given by ρ and modulated dynamically based on the proportion of exposed and—for constitutively immune scenarios, susceptible—cells in the system. We use ε to quantify the extent of induced versus constitutive immunity, with fully induced immunity corresponding to $\varepsilon = 0$ and maximally constitutive immunity to $\varepsilon = 1$.

We define "induced immunity" as complete, modeling all cells as susceptible to viral invasion at disease free equilibrium, with defenses induced subsequent to viral exposure. By contrast, we allow the extent of constitutive immunity to vary across parameter ranges, defining "constitutive" systems as those containing *any* antiviral cells at disease free equilibrium. Since the extent to which constitutively-expressed IFN-α is constitutively translated remains unknown

bioRxiv preprint doi: https://doi.org/10.1101/696195; this version posted July 8, 2019. The copyright holder for this preprint (which was not certified by peer review) is the author/funder, who has granted bioRxiv a license to display the preprint in perpetuity. It is made available under aCC-BY 4.0 International license.

for bat hosts (Zhou et al., 2016), this approach allows our tissue culture data to drive modeling inference: even in PaKiT01 cell lines known to constitutively express IFN-α ($\varepsilon = 1$), the true constitutive extent of the system (i.e. the quantity of antiviral cells present at disease free equilibrium) is still modulated by other antiviral rate parameters: ρ, μ, and *c* (the return rate of antiviral cells to susceptible status). We elected to estimate both the cell-to-cell transmission rate (β) and the rate of progression to antiviral status (ρ) by fitting our model to the statistical mean of infection trials, thus allowing the data to determine baseline antiviral status for each cell line.

Testable theoretical predictions.

Before fitting to empirical time series, we analyzed our theoretical model and generated testable hypotheses on the basis of model outcomes. From our within-host model system (equations 1-5), we derived the following expression for R_0, the pathogen basic reproduction number:

$$R_0 = \frac{\beta\sigma[b(c+\mu)-\mu(c+\mu+\varepsilon\rho)]}{b(\alpha+\mu)(\sigma+\mu)(c+\mu+\varepsilon\rho)} \quad (6)$$

Pathogens can invade a host tissue culture when $R_0 > 1$, which occurs when the numerator of the derived expression is positive. This requires the system to satisfy the following inequality:

$$b(c+\mu) > \mu(c+\mu+\varepsilon\rho) \quad (7)$$

For all systems with some degree of constitutive immunity ($\varepsilon > 0$ and $\rho > 0$), even when cell births (*b*) outpace deaths (μ), the inequality will be violated (and $R_0 < 1$) at large values of ε

bioRxiv preprint doi: https://doi.org/10.1101/696195; this version posted July 8, 2019. The copyright holder for this preprint (which was not certified by peer review) is the author/funder, who has granted bioRxiv a license to display the preprint in perpetuity. It is made available under aCC-BY 4.0 International license.

(highly constitutive interferon) or large values of ρ (rapid progression to antiviral status). In cases of fully induced or absent immunity ($\varepsilon = 0$), the R_0 equation reduces to a form typical of the classic SEIR model:

$$R_0 = \frac{\beta\sigma(b-\mu)}{b(\alpha+\mu)(\sigma+\mu)} \tag{8}$$

Here, a positive numerator is achieved under conditions permitting cell growth ($b > \mu$). Regardless of immune assumptions, pathogen invasion is favored when transmission (β) outpaces cell death, both natural (μ) and pathogen-induced (α).

At equilibrium, the mean field model demonstrates one of three infection states: endemic equilibrium, stable limit cycles, and no infection (Figure 2). Respectively, these states approximate the persistent infection, virus-induced epidemic extinction, and immune-mediated epidemic extinction phenotypes previously witnessed in tissue culture experiments (Figure 1). Theoretically, endemic equilibrium is maintained when new infections are generated at the same rate at which infections are lost, while limit cycles represent parameter space under which infectious and susceptible populations are locked in predictable oscillations. Endemic equilibriums resulting from cellular regeneration (i.e. births) have been described *in vivo* for HIV (Coffin, 1995) and *in vitro* for herpesvirus plaque assays (Howat et al., 2006), but true limit cycles likely only occur theoretically.

bioRxiv preprint doi: https://doi.org/10.1101/696195; this version posted July 8, 2019. The copyright holder for this preprint (which was not certified by peer review) is the author/funder, who has granted bioRxiv a license to display the preprint in perpetuity. It is made available under aCC-BY 4.0 International license.

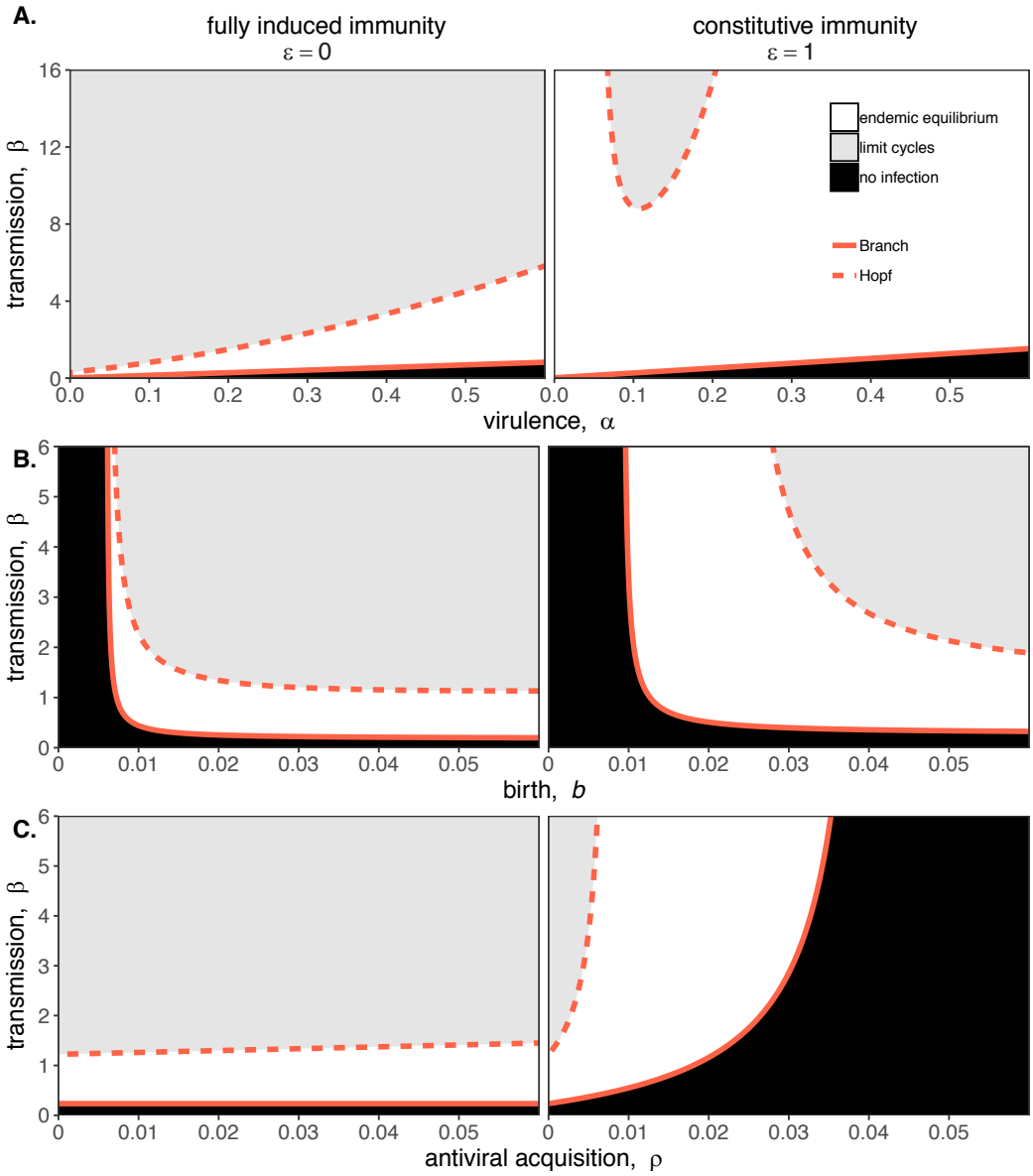

Figure 2. Two parameter bifurcations of the mean field model, showing equilibrium dynamics under fully induced ($\varepsilon = 0$) and maximally constitutive ($\varepsilon = 1$) immunity, across variations in the transmission rate, β, coupled with variations in the rates for (A) pathogen-induced mortality, α, (B) birth, *b*, and (C) progression to antiviral status, ρ. Axes are different for panel (A) versus (B) and (C). Branching point curves are represented as solid lines and Hopf curves as dashed lines. White space indicates endemic equilibrium (persistence), gray space indicates limit cycling, and black space indicates no infection (extinction). Unless varied along axes, $b = .025$, $\mu = 1/168$, $\sigma = 1/6$, $c = 1/144$, $\alpha = 1/6$, $\rho = .007$.

bioRxiv preprint doi: https://doi.org/10.1101/696195; this version posted July 8, 2019. The copyright holder for this preprint (which was not certified by peer review) is the author/funder, who has granted bioRxiv a license to display the preprint in perpetuity. It is made available under aCC-BY 4.0 International license.

Bifurcation analysis of our mean field model reveals that regions of no infection (pathogen extinction) are typically bounded at lower threshold (Branching point) values for β, below which the pathogen is unable to invade. We find no upper threshold to invasion for β under any circumstances (i.e. β high enough to drive pathogen-induced extinction), but high β values result in Hopf bifurcations, which delineate regions of parameter space characterized by limit cycles. Since limit cycles only occur theoretically, high βs recovered in this range will likely produce virus-induced epidemic extinction under experimental conditions. Hopf bifurcations occur at higher values for β under constitutive versus induced immune conditions, permitting endemic persistence at higher viral replication rates. Differences observed under induced and constitutive immune assumptions are intensified at higher values for ρ.

In regions of parameter space corresponding to endemic persistence, a given transmission rate (β) corresponds to a lower virulence (α) when comparing cases of constitutive versus induced immunity (Figure 2A). Constitutive immunity enables endemic persistence at extremely high values for β when paired with intermediate birth rates (Figure 2B), while equivalent parameter combinations under fully induced immunity localize in the limit cycle region for deterministic equilibrium—likely to produce stochastic experimental extinctions. In contrast, constitutive immune assumptions result in higher threshold birth rates (Branching points), below which the pathogen is unable to invade, than do induced assumptions. Consistent with our derivation for R_0, we find that, under induced immune assumptions, viral invasion is independent of antiviral dynamics, while, under constitutive immune assumptions, there is a maximum threshold rate of acquisition to antiviral status (ρ), above which viral invasion, even at high transmission rates (β), is not permitted.

bioRxiv preprint doi: https://doi.org/10.1101/696195; this version posted July 8, 2019. The copyright holder for this preprint (which was not certified by peer review) is the author/funder, who has granted bioRxiv a license to display the preprint in perpetuity. It is made available under aCC-BY 4.0 International license.

Fitting of theoretical model to cell culture data demonstrates higher within-host transmission rates under constitutive immune assumptions.

To estimate within-host viral transmission rates (β) and rates of cellular acquisition to antiviral status (ρ), we next fit our mean field theoretical model to each unique cell line-virus-MOI time series, under absent, induced, and constitutive assumptions of immunity. Parameter estimates resulting from least squares model fitting to MOI=0.001 data are visualized in conjunction with β – ρ bifurcations in Figure 3; all general patterns were recapitulated at lower values for β on MOI=0.0001 trials (SI Appendix, Figure S4). We used the localization of parameter estimates on β – ρ bifurcations to classify each unique cell-virus epidemic according to equilibrium properties of the deterministic model. We consistently estimated higher β-values and 10-fold lower ρ-values under constitutive versus induced immunity for the same cell-virus combination (Figure 3; SI Appendix, Figure S4, Table S3).

Table 1. Optimized parameters from best fit deterministic model and spatial approximation

Cell Line	Virus	Mean Field Model			Spatial Model		
		Immunity (ε)	ρ [lci – uci] †	β [lci – uci] †	Immunity (ε)	ρ	β [lci – uci] †
Vero	rVSV-G	Absent* (ε=0)	0 [0-0]	1.56 [0-3.61]	Absent* (ε=0)	0	620 [19.7-1220]
	rVSV-EBOV	Absent* (ε=0)	0 [0-0]	1.02 [0-2.5]	Absent* (ε=0)	0	927 [578-1280]
	rVSV-MARV	Absent* (ε=0)	0 [0-0]	0.588 [0.126-1.05]	Absent* (ε=0)	0	2.68 [0-18.2]
RoNi/7.1	rVSV-G	Induced* (ε=0)	0.108 [0-1.31]	1.86 [0-4.35]	Absent* (ε=0)	0	628 [0-1280]
	rVSV-EBOV	Induced* (ε=0)	0.111 [0-1.27]	0.724 [0-1.65]	Constitutive*** (ε=1)	0.000253	2.68 [0-11.1]
	rVSV-MARV	Induced* (ε=0)	0.0348 [0-0.92]	1.13 [0-2.42]	Absent* (ε=0)	0	547 [0-1100]
PaKiT01	rVSV-G	Induced* (ε=0)	0.44 [0-3.07]	2.12 [0-6.37]	Induced* (ε=0)	0.44	136 [0-574]

bioRxiv preprint doi: https://doi.org/10.1101/696195; this version posted July 8, 2019. The copyright holder for this preprint (which was not certified by peer review) is the author/funder, who has granted bioRxiv a license to display the preprint in perpetuity. It is made available under aCC-BY 4.0 International license.

	rVSV-EBOV	Induced* (ε=0)	0.155 [0-2.25]	0.549 [0-2.48]	Constitutive*** (ε=1)	0.0129	6.02 [0-18.5]
	rVSV-MARV	Induced* (ε=0)	14.2 [0-48.4]	2.75 [0-33.5]	Induced* (ε=0)	14.3	9.36 [0-19.3]

*Immune Absent scenarios: b=.025, μ= 1/168, σ = 1/6, α = 1/6, c=0, ε = 0
**Induced Immunity scenarios: b=.025, μ = 1/168, σ = 1/6, α= 1/6, c = 1/144, ε = 0
***Constitutive Immunity scenarios: b=.025, μ = 1/168, σ = 1/6, α= 1/6, c = 1/144, ε = 1
†lci = lower and uci = upper 95% confidence interval. No confidence interval is shown for spatial ρ, which was fixed.

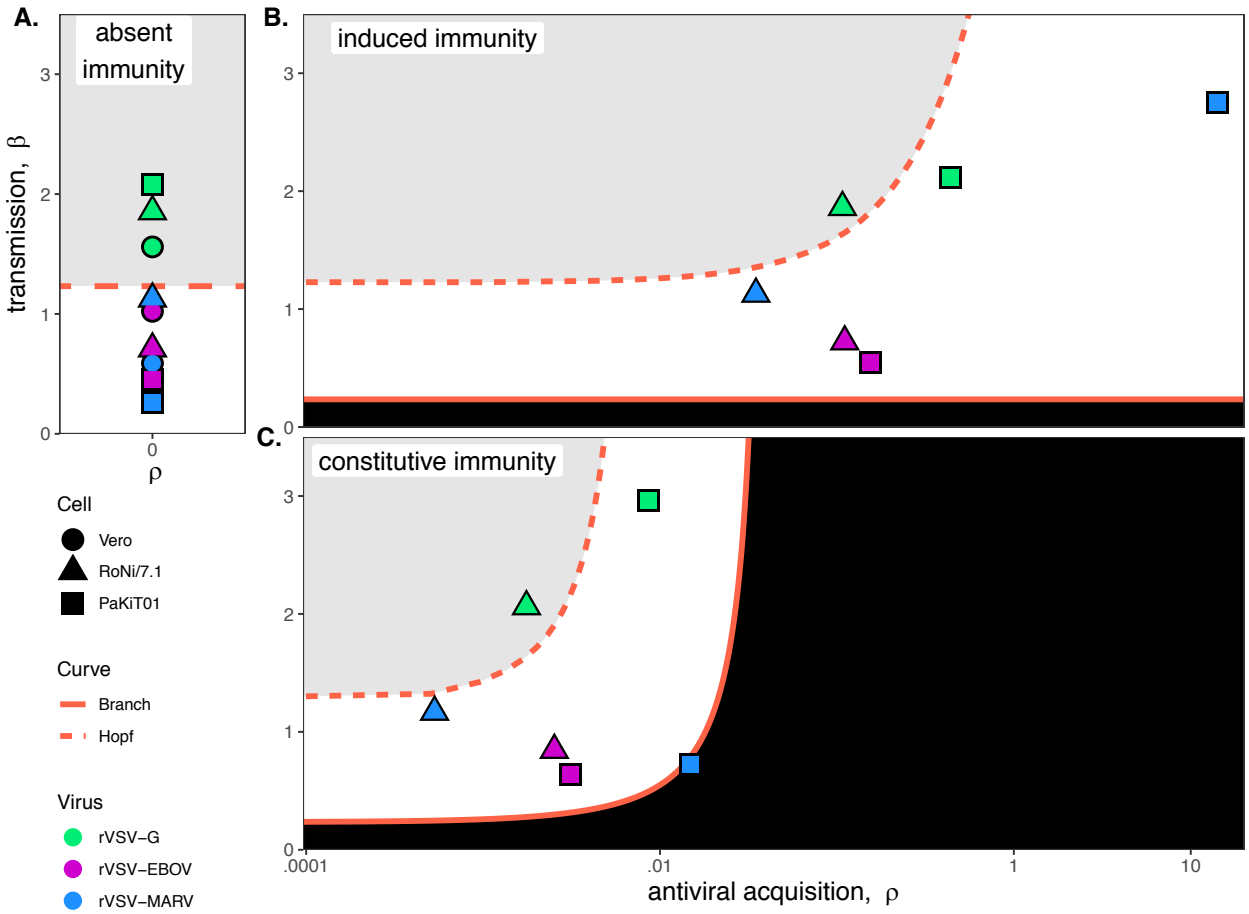

Figure 3. Parameter estimates for β and ρ from mean-field model fits to MOI=0.001 time series data, atop β – ρ bifurcation. Fits and bifurcations are grouped by immune phenotype: (A) absent; (B) induced; (C) constitutive immunity, with cell lines differentiated by shape (Vero=circles; RoNi/7.1 = triangles; PaKiT01=squares) and viral infections by color (rVSV-G = green, rVSV-EBOV = magenta, rVSV-MARV = blue). Branch Point curves (solid lines) and Hopf curves (dashed lines) are reproduced from Figure 2C, though the x-axis is shown here on a log-scale. White space indicates endemic equilibrium (pathogen persistence), gray space indicates limit

bioRxiv preprint doi: https://doi.org/10.1101/696195; this version posted July 8, 2019. The copyright holder for this preprint (which was not certified by peer review) is the author/funder, who has granted bioRxiv a license to display the preprint in perpetuity. It is made available under aCC-BY 4.0 International license.

cycling, and black space indicates no infection (pathogen extinction). Parameter values: $b = .025$, $\mu = 1/168$, $\sigma = 1/6$, and $\alpha = 1/6$. Raw fitted values and corresponding 95% confidence intervals for β and ρ, background parameter values, and AIC recovered from model fit, are reported in Table S3. Parameter fits at MOI=0.0001 are visualized in SI Appendix, Figure S4.

We fit Vero cell data with an absent immunity model only (Figure 3A). Among Vero cell trials, infections with rVSV-G produced the highest β estimates, corresponding to limit cycle dynamics in theoretical parameter space (likely to yield virus-induced epidemic extinction under stochastic, experimental conditions). Lower β values were recovered for rVSV-EBOV and rVSV-MARV on Vero cells; both localized in the parameter range of endemic equilibrium for the deterministic model, though at low equilibrium infectious proportions (Figure 4).

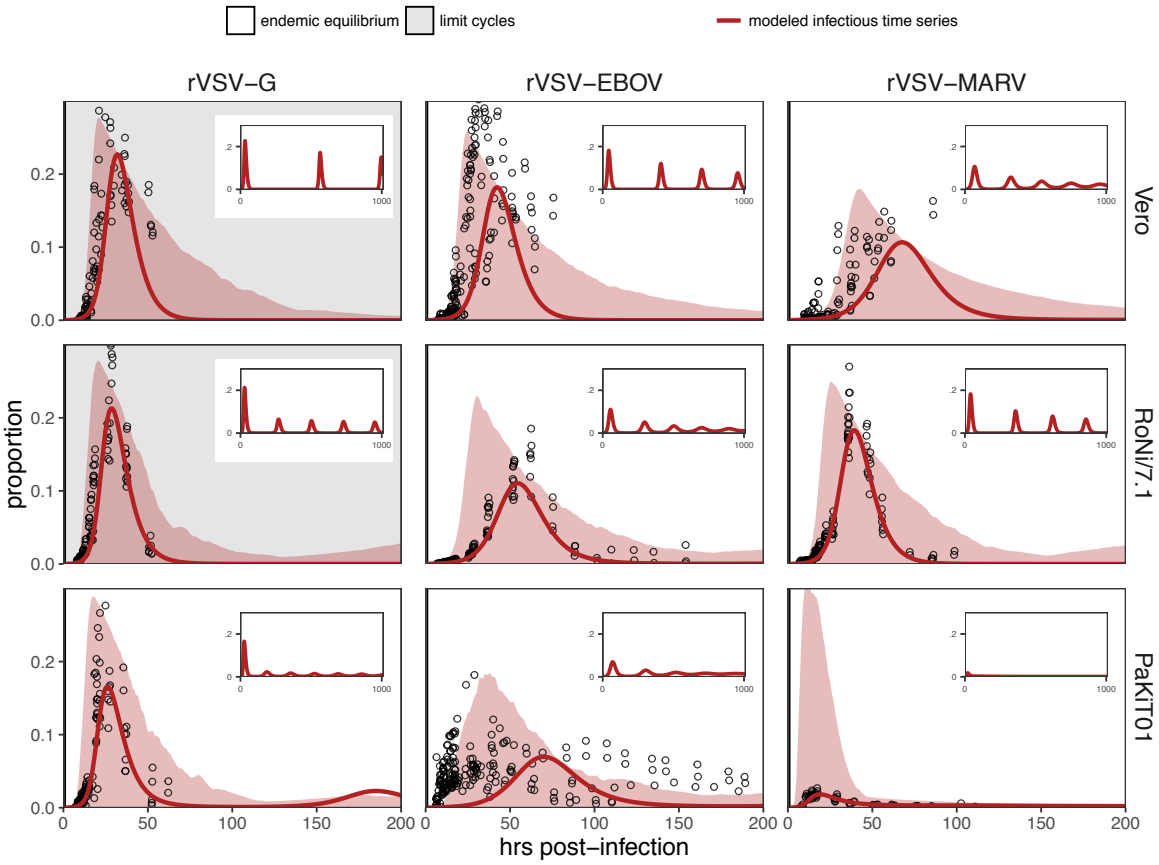

bioRxiv preprint doi: https://doi.org/10.1101/696195; this version posted July 8, 2019. The copyright holder for this preprint (which was not certified by peer review) is the author/funder, who has granted bioRxiv a license to display the preprint in perpetuity. It is made available under aCC-BY 4.0 International license.

Figure 4. Fitted time series of infectious cell proportions from mean field model for rVSV-G, rVSV-EBOV, and rVSV-MARV infections (columns) on Vero, RoNi/7.1, and PaKiT01 cell lines (rows) at MOI=0.001. Results are shown for the best fit immune absent model on Vero cells and induced immunity model on RoNi/7.1 and PaKiT01 cells. Raw data across all trials are shown as open circles and model output as a solid crimson line (95% confidence intervals by standard error = red shading). Inset panels within each facet show theoretical result of 1000 hours of deterministic model simulation under corresponding parameter combinations. Panel background corresponds to equilibrium state of the dynamical system (endemic equilibrium = white; limit cycles = gray). Parameter values are listed in Table 1 and S3. Results for absent/induced/constitutive fitted models across all cell lines are shown in SI Appendix, Figure S5 (MOI=0.001) and S6 (MOI=0.0001).

We fit RoNi/7.1 and PaKiT01 cell data with all three absent, induced, and constitutive models of immunity (Figure 3; SI Appendix, Figure S4). Consistent with reported patterns in the literature and our own validation by qPCR (SI Appendix, Figure S2), the induced immunity model offered the best fit to all RoNi/7.1 data—though ρ-values optimized under constitutive assumptions were so low that the ratio of equilibrium antiviral to susceptible proportions (P_A* : P_S*) was close to 0 in all cases, meaning that constitutive antiviral defenses qualitatively replicated induced conditions (SI Appendix, Table S3). In all RoNi/7.1 scenarios, we estimated highest β values for rVSV-G infections; in contrast to Vero cells, we recovered higher β estimates for rVSV-MARV than for rVSV-EBOV, both of which were localized as endemic equilibriums (again at low infectious proportions). This reversal was balanced by a higher estimated rate of acquisition to antiviral status (ρ) for rVSV-EBOV versus rVSV-MARV in both induced and constitutive immune models (Figure 3B/C).

As with RoNi/7.1 data, all PaKiT01 data were best fit by induced immunity models, though idiosyncratic parameter estimates for PaKiT01-rVSV-MARV infections suggest that this cell-virus combination may be better described at an intermediate value of ε (SI Appendix, Table S3). Such results are consistent with reports in the literature indicating that, despite constitutive expression of IFN-α (Zhou et al., 2016), additional antiviral defenses may still be induced upon

bioRxiv preprint doi: https://doi.org/10.1101/696195; this version posted July 8, 2019. The copyright holder for this preprint (which was not certified by peer review) is the author/funder, who has granted bioRxiv a license to display the preprint in perpetuity. It is made available under aCC-BY 4.0 International license.

viral challenge in PaKiT01 cell lines. Experimental time series for PaKiT01 spanned the full suite of equilibrium outcomes, with rVSV-G infections producing virus-induced epidemic extinctions, rVSV-EBOV infections resulting in persistent infections, and rVSV-MARV infections yielding immune-mediated epidemic extinction (Figure 4).

Consistent with previous results, under immune absent conditions, β-values were estimated highest for rVSV-G infections on PaKiT01, producing limit cycle localizations in parameter space (Figure 3A). Under both immunity-permitting models, rVSV-G fits localized in the endemic equilibrium region for PaKiT01, and comparable dynamics were recovered under induced and constitutive assumptions, with ρ approximately ten-fold lower when some constitutive defenses were permitted than when all defenses were induced. In tissue culture, rVSV-EBOV infections on PaKiT01 produced the one apparently persistent infection recovered in our tissue culture trials. Under both assumptions of induced and constitutive immunity, we modeled this phenotype at relatively low estimates for ρ paired with low estimates for β. Experimentally, rVSV-MARV infections yielded immune-induced epidemic extinctions on PaKiT01 cells (Figure 1); induced and constitutive mean field models offered comparable fits to these data, with ten-fold lower estimates for ρ in constitutive cases. However, the induced immunity estimate for β was aberrantly higher than the constitutive, a result of the deterministic model's inability to replicate immune-mediated epidemic extinction at $\varepsilon = 0$. Consistent with our derivation for R_0, the phenotype of immune-induced extinction was largely mediated by ρ regardless of the value for β. Under constitutive immune assumptions, β – ρ estimates localized along the threshold Branching point curve delineating pathogen extinction (Figure 3C); parameter estimation saturated at maximal values for ρ which satisfied conditions for pathogen invasion ($R_0 \geq 1$; Equation 7).

bioRxiv preprint doi: https://doi.org/10.1101/696195; this version posted July 8, 2019. The copyright holder for this preprint (which was not certified by peer review) is the author/funder, who has granted bioRxiv a license to display the preprint in perpetuity. It is made available under aCC-BY 4.0 International license.

Total monolayer destruction occurred in all cell-virus combinations excepting rVSV-EBOV infections on RoNi/7.1 cells and rVSV-EBOV and rVSV-MARV infections on PaKiT01 cells, signifying susceptible depletion concomitant with epidemic turnover, as indicated when R-effective (the product of R_0 and P_S) was reduced below one (Figure 5). For rVSV-EBOV infections on RoNi/7.1, induced antiviral cells safeguarded remnant live cells late in the time series, allowing for susceptible regeneration. In rVSV-EBOV and rVSV-MARV infections on PaKiT01 cells, Figure 5 demonstrates how declining susceptibles were replaced by antiviral cells such that the epidemic was halted (R-effective <1) before susceptibles declined. In the case of rVSV-EBOV on PaKiT01, this facilitated long-term epidemic persistence as remnant susceptibles continued to reproduce and eventually undergo infection themselves. In rVSV-MARV infections, by contrast, antiviral cells replaced susceptible cells so rapidly that the remnant susceptible population was too small to support enough new births to maintain transmission before epidemic extinction.

bioRxiv preprint doi: https://doi.org/10.1101/696195; this version posted July 8, 2019. The copyright holder for this preprint (which was not certified by peer review) is the author/funder, who has granted bioRxiv a license to display the preprint in perpetuity. It is made available under aCC-BY 4.0 International license.

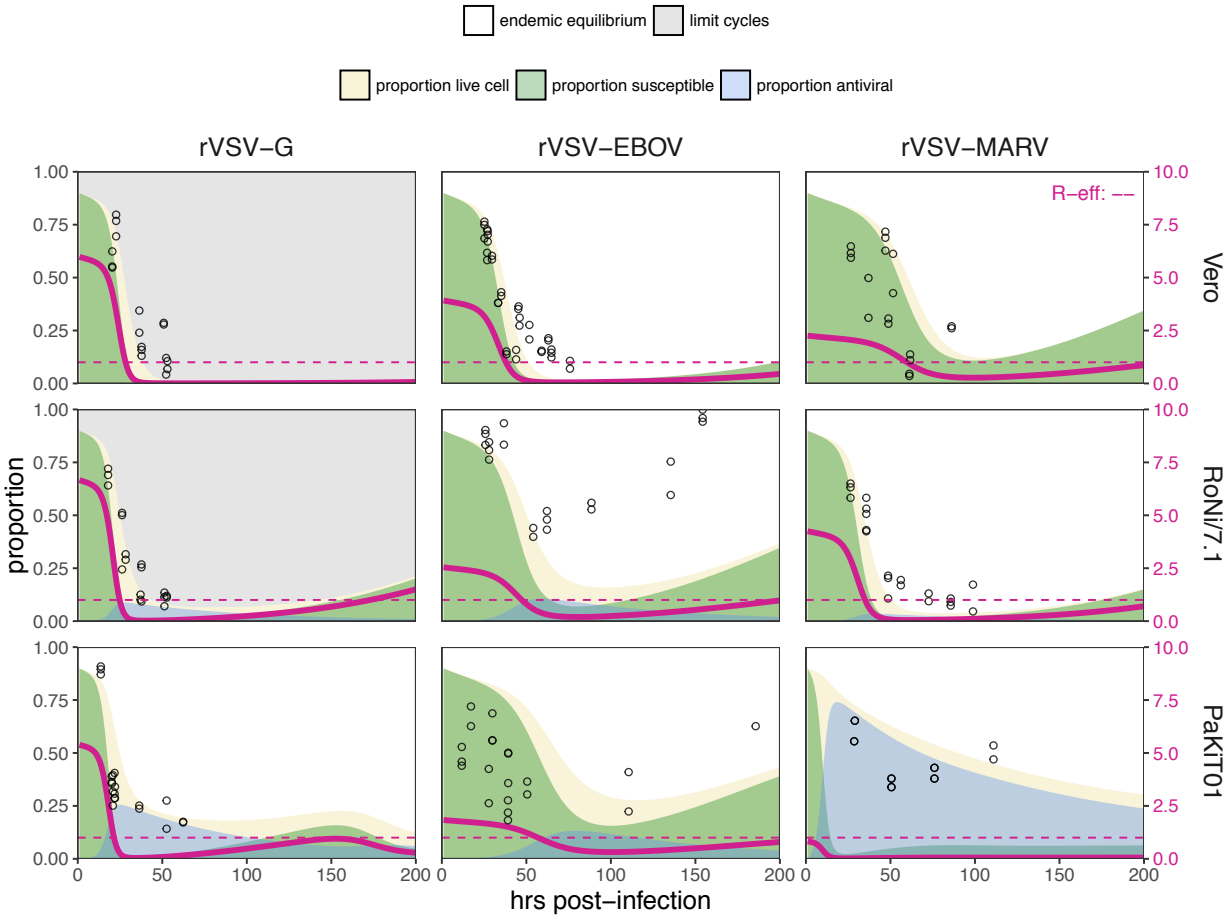

Figure 5. Fitted time series of susceptible (green shading) and antiviral (blue shading) cell proportions from the mean field model for rVSV-G, rVSV-EBOV, and rVSV-MARV infections (columns) on Vero, RoNi/7.1, and PaKiT01 cell lines (rows) at MOI=0.001. Results are shown for the best fit immune absent model on Vero cells, and induced immunity model on RoNi/7.1 and PaKiT01 cells. Combined live, uninfectious cell populations (S + A + E) are shown in tan shading, with raw live, uninfectious cell data from DaPi stains of terminal time series visualized as open circles. The right-hand y-axis corresponds to R-effective (pink solid line) across each time series; R-effective =1 is a pink dashed, horizontal line. Panel background corresponds to equilibrium state of the dynamical system (endemic equilibrium = white; limit cycles = gray). Parameter values are listed in SI Appendix, Table S3 and results for absent/induced/constitutive fitted models across all cell lines in Figure S7 (MOI=0.001) and S8 (MOI=0.0001).

Model fitting results are validated and intensified under spatial conditions.

Because the agar overlay of a plaque assay restricts infection to two dimensions, we at last investigated whether our inference into within-host viral dynamics could be improved by a spatially-explicit recapitulation of our data. We modeled the same five epidemic states

bioRxiv preprint doi: https://doi.org/10.1101/696195; this version posted July 8, 2019. The copyright holder for this preprint (which was not certified by peer review) is the author/funder, who has granted bioRxiv a license to display the preprint in perpetuity. It is made available under aCC-BY 4.0 International license.

(susceptible, antiviral, exposed, infectious, and dead) from our mean field model on a two-dimensional hexagonal lattice, with cell state transitions governed probabilistically (Howat et al., 2006; Nagai & Honda, 2001). We found that the spatial stochastic model more effectively reproduced experimental trials than the deterministic mean field model, with the strongest support recovered for immune absent assumptions in all Vero cell trials and in rVSV-G and rVSV-MARV infections on RoNi/7.1 cell lines, for induced immune assumptions in rVSV-G and rVSV-MARV infections on PaKiT01 cell lines, and for constitutive immune assumptions in rVSV-EBOV infections on RoNi/7.1 and PaKiT01 cell lines (Figure 6).

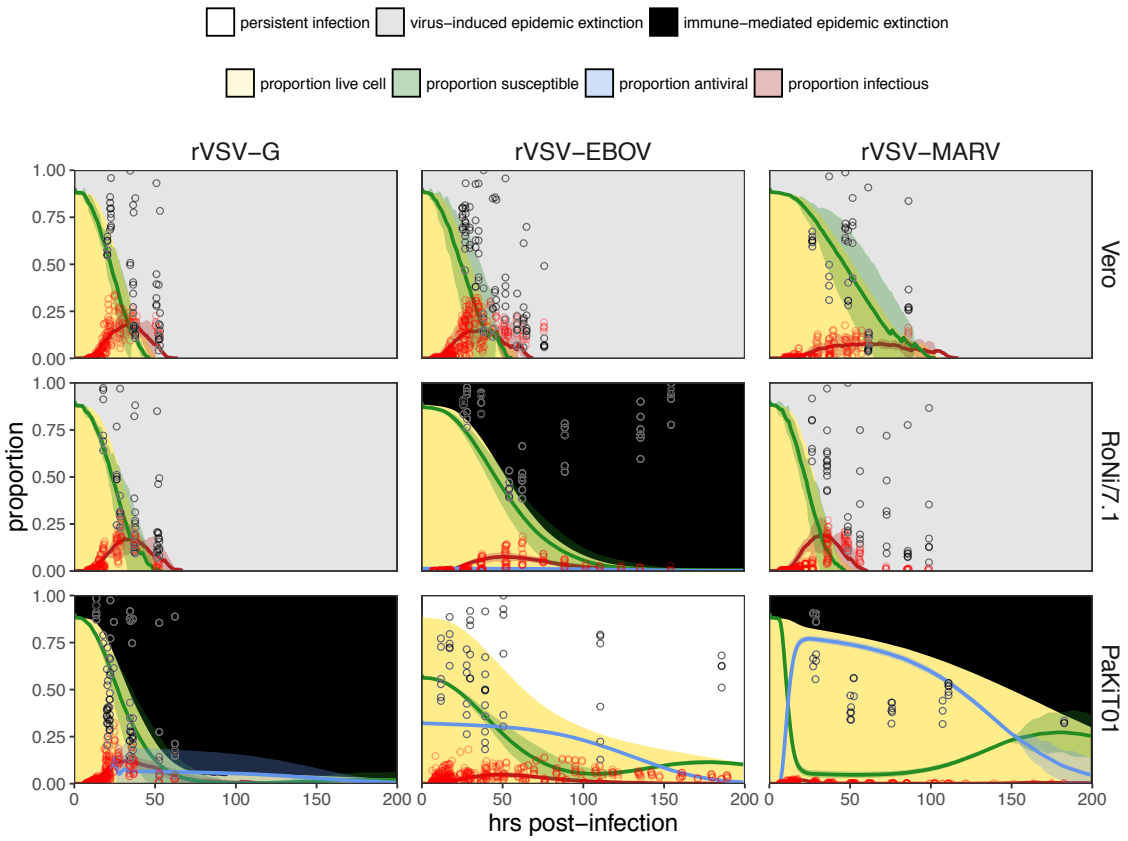

Figure 6. Best fit stochastic spatial model outcomes for each cell line–virus combination: the immune absent model for Vero cells and for rVSV-G and rVSV-MARV infections on RoNi/7.1 cells, the induced immunity model for rVSV-G and rVSV-MARV infections on PaKiT01 cells, and the constitutive immunity model for rVSV-EBOV infections on RoNi/7.1 and PaKiT01

bioRxiv preprint doi: https://doi.org/10.1101/696195; this version posted July 8, 2019. The copyright holder for this preprint (which was not certified by peer review) is the author/funder, who has granted bioRxiv a license to display the preprint in perpetuity. It is made available under aCC-BY 4.0 International license.

cells. We show the mean output from 10 runs of the spatial stochastic model, on a 10,000 cell lattice for MOI=0.001. Mean state variable outputs are plotted as colored lines with 95% confidence intervals by standard error shown in corresponding shading (infectious = red; susceptible = green; antiviral = blue). Raw infectious cell data across all time trials are plotted as open red circles, with DaPi-stain infectious live cell population as open black circles. Modeled live, uninfectious cell populations (S+A+E) are shown in tan shading in the background. Panel background shading corresponds to the mean spatial model outcome for each cell line–virus combination (persistent infection = white; virus-induced epidemic extinction = gray; immune-mediated epidemic extinction = black)*. Parameter values are reported in Table 1 and in SI Appendix, Table S4. Results for all absent/induced/constitutive fitted models across all cell lines are depicted in SI Appendix, Figure S9. **Note that persistent infection was classified as any model which maintained infectious cells at the end of the time series in more than one stochastic run, while immune-mediated epidemic extinction was classified as any model which maintained susceptible and antiviral cells but no infectious cells at the end of the time series in more than half of all stochastic runs.*

Spatial fits produced β estimates several orders of magnitude higher than those recovered under mean field conditions (Table 1; SI Appendix, Table S4), an unsurprising result, given that spatial structure is known to intensify parameter thresholds permitting pathogen invasion (Webb, Keeling, & Boots, 2007). Spatial structure further intensified antiviral cell contributions to endemic persistence in tissue culture. Persistent infections established for our mean field model under conditions in which antiviral cell populations protected live cells through the initial epidemic invasion, such that the infection was "re-seeded" as antiviral cells returned to susceptibility later in the time series (Figure 5). The same occurred even more explicitly in a spatial context: antiviral cells acted as 'refugia' which protected live cells from infection as each initial epidemic wave 'washed' across a cell monolayer (Figure 6; SI Appendix, Video S1-S3). Eventual return of these antiviral cells to susceptible status allowed for sustained epidemic transmission in cases where some infectious cells persisted at later timepoints in simulation.

On RoNi/7.1 cell lines, both mean field and spatial models were consistent in demonstrating more virulent epidemics for rVSV-G and rVSV-MARV versus rVSV-EBOV infections, though no host immune response was required to dampen the epidemic curve for these virulent infections in the slower-spreading spatially-structured context. As innate immune

bioRxiv preprint doi: https://doi.org/10.1101/696195; this version posted July 8, 2019. The copyright holder for this preprint (which was not certified by peer review) is the author/funder, who has granted bioRxiv a license to display the preprint in perpetuity. It is made available under aCC-BY 4.0 International license.

mechanisms for RoNi/7.1 cell lines are known to be idiosyncratic (Arnold et al., 2018; Biesold et al., 2011; Kühl et al., 2011; Kuzmin et al., 2017; Omatsu et al., 2008; Pavlovich et al., 2018), our results are consistent with the literature and suggest a less pronounced role for interferon defense against viral infection in RoNi/7.1 versus PaKiT01 cells. Spatial fits for PaKiT01 data were largely consistent with mean field model results, showing strongest support for induced immune assumptions, with the exception of fits to persistent rVSV-EBOV infections, for which constitutive assumptions performed better. These results further highlight the key role which remnant antiviral cells appear to play in maintaining endemic infections. In all cases, the spatial model effectively recapitulated stochastic extinctions witnessed in experimental tissue cultures, which could not be achieved in a deterministic model framework.

Discussion

Bats are reservoirs for highly virulent emerging human infections, but the mechanisms by which they host their pathogens have not been well elucidated. We used an innovative combination of *in vitro* experimentation and within-host modeling to explore these mechanisms under contrasting assumptions of induced and constitutive immunity. Critically, we found that induced immune responses favor slower cell-to-cell transmission rates (a proxy for viral replication rates) paired with more rapid rates of cellular acquisition of antiviral immunity, while constitutive immunity amplifies cellular transmission rates, in conjunction with less rapid antiviral responses. These findings have important consequences for understanding pathogen virulence evolution in reservoir hosts possessing constitutively antiviral immune capacities (i.e. bats)—especially when considering the consequences of pathogen emergence into secondary

bioRxiv preprint doi: https://doi.org/10.1101/696195; this version posted July 8, 2019. The copyright holder for this preprint (which was not certified by peer review) is the author/funder, who has granted bioRxiv a license to display the preprint in perpetuity. It is made available under aCC-BY 4.0 International license.

host populations. If hosts with constitutive immune defenses favor evolution of rapidly transmitting viruses, such pathogens are likely to cause extreme virulence in spillover hosts lacking similarly constitutive defenses.

To elucidate the role of innate immunity in promoting or preventing long-term viral persistence within bat hosts, we developed a within-host model of bat viral dynamics *in vitro*, then fit this model to experimental data from viral infections on cell lines expressing induced and constitutive immune phenotypes. From our theoretical model, we derived an equation for R_0, the basic reproduction number for the virus, which demonstrates how constitutive immune defenses elevate threshold requirements for pathogen invasion, with viral propagation deterred in host cells exhibiting slow birth rates, b, or fast antiviral response rates, ρ. No matter how rapid, induced defenses are incapable of preventing viral invasion in our deterministic model. Bifurcation analysis of our theoretical model demonstrates that once thresholds for pathogen invasion have been met, assumptions of constitutive immunity appear to limit the cellular mortality (virulence) incurred at high transmission rates, β, consequently favoring faster cell-to-cell viral transmission.

Our theoretical results were supported by *in vitro* investigations into the influence of innate immune processes on viral persistence. Modeling indicated that viral persistence was attainable under both induced and constitutive assumptions of immunity, but, consistent with our original hypotheses, mean field models assuming induced immunity offered the best recapitulation of empirical data, including that derived from *P. alecto* cell lines, which constitutively express the antiviral cytokine, IFN-α (Zhou et al., 2016). This support for induced immunity suggests that IFN-α expression in *P. alecto* cells may represent more of a constitutive immune priming process than a perpetual, functional, antiviral defense. Nonetheless, spatial

bioRxiv preprint doi: https://doi.org/10.1101/696195; this version posted July 8, 2019. The copyright holder for this preprint (which was not certified by peer review) is the author/funder, who has granted bioRxiv a license to display the preprint in perpetuity. It is made available under aCC-BY 4.0 International license.

model support for constitutive immune assumptions in this same context highlights the efficiency of this primed host cell response versus the conventional induced response exhibited in *R. aegyptiacus* cells and further emphasizes the key role which antiviral cells—whether induced or constitutive—appear to play in maintaining endemic infections.

Our tissue culture experiments also showed the unique capacity of constitutive immune defenses to deter viral invasion altogether. Regardless of interferon phenotype, we know PaKiT01 cells to be constitutively refractory to infection with rVSV-MARV due to receptor-level incompatibilities (Ng & Chandran, 2018). In our experiments, baseline constitutive immunity in PaKiT01 cells challenged with rVSV-MARV resulted in immune-mediated epidemic extinctions across experimental trials. Despite known cell line-virus incompatibilities, our theoretical model recapitulated these data under induced immune assumptions. This result is likely due to deterministic modeling constraints: viral invasion requires $R_0 \geq 1$, but cell culture trials nonetheless went consistently extinct, suggesting empirical R_0 to be < 1. In spatial model fits to rVSV-MARV infections on PaKiT01 cells, we also recovered stronger support for induced versus constitutive immune assumptions—again because infection was unable to effectively invade the constitutively antiviral model system.

Critical community size describes the empirical stochastic persistence threshold, a minimum host population supporting long term pathogen maintenance (Bartlett, 1957). For all cases in which $R_0 > 1$, deterministic epidemiological models will converge on a steady state endemic value for the equilibrium number of infectious individuals, or settle into a cyclic epidemic trajectory. Thus, if the pathogen can invade, it will persist—a result we consistently recovered when fitting our mean field model to tissue culture data, despite the fact that most of our epidemics went extinct *in vitro*. In reality, low host population sizes and correspondingly low

bioRxiv preprint doi: https://doi.org/10.1101/696195; this version posted July 8, 2019. The copyright holder for this preprint (which was not certified by peer review) is the author/funder, who has granted bioRxiv a license to display the preprint in perpetuity. It is made available under aCC-BY 4.0 International license.

infectious proportions make populations vulnerable to chance events that result in infection extinction—like those witnessed in cell culture data and stochastic model fits (SI Appendix, Video S1-S3). As previously demonstrated in within-host models for HIV (Bonhoeffer, May, Shaw, & Nowak, 1997; Coffin, 1995; Nowak et al., 1995; A S Perelson, Neumann, Markowitz, Leonard, & Ho, 1996), assumptions of simple target-cell depletion can often provide satisfactory approximations of viral dynamics, especially those reproduced in simple *in vitro* systems. Critically, fitting of our spatial model emphasized the important role of host antiviral immunity in dampening those epidemics in *P. alecto* cell cultures, including those suggestive of persistent infection. Nonetheless, we acknowledge the limitations imposed by *in vitro* experiments in tissue culture, especially involving recombinant viruses and immortalized cell lines. At a minimum, future work should extend these cell cultures to include measurements of multiple state variables (i.e. antiviral cells).

The continued recurrence of Ebola epidemics across central Africa highlights the importance of understanding bats' roles as reservoirs for virulent zoonotic disease. The past decade has born witness to emerging consensus regarding the unique pathways by which bats resist and tolerate highly virulent infections (Ahn et al., 2019; Brook & Dobson, 2015; Ng et al., 2015; Pavlovich et al., 2018; Xie et al., 2018; Zhang et al., 2013; Zhou et al., 2016), but an understanding of the mechanisms by which bats support endemic pathogens at the population level, or promote the evolution of virulent pathogens at the individual level, remains elusive. Endemic maintenance of infection is a defining characteristic of a pathogen reservoir (Haydon et al., 2002), and bats appear to merit such a title, supporting long-term persistence of highly transmissible viral infections in isolated island populations well below expected critical community sizes (Peel et al., 2012). Researchers debate the relative influence of population-level

bioRxiv preprint doi: https://doi.org/10.1101/696195; this version posted July 8, 2019. The copyright holder for this preprint (which was not certified by peer review) is the author/funder, who has granted bioRxiv a license to display the preprint in perpetuity. It is made available under aCC-BY 4.0 International license.

and within-host mechanisms which might explain these trends (Plowright et al., 2016), but increasingly, field data are difficult to reconcile without acknowledgement of a role for persistent infections (Brook et al., 2019; Peel et al., 2018). We present general methods to study cross-scale viral dynamics, suggesting that within-host persistence can be supported under conditions of both induced and constitutive innate immunity. Viruses which evolve rapid replication rates under constitutive host defenses, such as those described for bats, may pose the greatest hazard for cross-species pathogen emergence into spillover hosts.

bioRxiv preprint doi: https://doi.org/10.1101/696195; this version posted July 8, 2019. The copyright holder for this preprint (which was not certified by peer review) is the author/funder, who has granted bioRxiv a license to display the preprint in perpetuity. It is made available under aCC-BY 4.0 International license.

Methods

Cell Culture Experiments.

Cells.

All experiments were carried out on three immortalized mammalian kidney cell lines: Vero (African green monkey), RoNi/7.1 (*Rousettus aegyptiacus*) (Biesold et al., 2011; Kühl et al., 2011) and PaKiT01 (*Pteropus alecto*) (Crameri et al., 2009). The species identification of all cell lines was confirmed in the publication in which it was described. Monolayers of each cell line were grown to 90% confluency (~9 x 10^5 cells) in 6-well plates. Cells were maintained in a humidified 37˚C, 5% CO_2 incubator and cultured in Dulbecco's modified Eagle medium (DMEM) (Life Technologies, Grand Island, NY), supplemented with 2% fetal bovine serum (FBS) (Gemini Bio Products, West Sacramento, CA), and 1% penicillin-streptomycin (Life Technologies).

Previous work has demonstrated that all cell lines used are capable of mounting a type I IFN response upon viral challenge, with the exception of Vero cells, which possess an IFN-β deficiency (Desmyter et al., 1968; Emeny & Morgan, 1979; Rhim, Schell, Creasy, & Case, 1969). RoNi/7.1 cells have been shown to mount induced defenses upon viral infection (Biesold et al., 2011; Pavlovich et al., 2018), while PaKiT01 cells are known to constitutively express the antiviral cytokine, IFN-α (Zhou et al., 2016). This work is the first documentation of IFN signaling induced upon challenge with the particular recombinant VSVs outlined below. We verified known antiviral immune phenotypes via qPCR.

bioRxiv preprint doi: https://doi.org/10.1101/696195; this version posted July 8, 2019. The copyright holder for this preprint (which was not certified by peer review) is the author/funder, who has granted bioRxiv a license to display the preprint in perpetuity. It is made available under aCC-BY 4.0 International license.

Viruses.

Replication-capable recombinant vesicular stomatitis Indiana viruses, expressing filovirus glycoproteins in place of wild type G (rVSV-G, rVSV-EBOV, and rVSV-MARV) have been previously described (Miller et al., 2012; Wong et al., 2010). To measure infectivities of rVSVs on each of the cell lines outlined above, in order to calculate the correct viral dose for each MOI, NH_4Cl (20 mM) was added to infected cell cultures at 1–2 hours post-infection to block viral spread, and individual eGFP-positive cells were manually counted at 12–14 hours post-infection.

Innate Immune Phenotypes via qPCR of IFN Genes.

Previously published work indicates that immortalized kidney cell lines of *Rousettus aegyptiacus* (RoNi/7.1) and *Pteropus alecto* (PaKiT01) exhibit different innate antiviral immune phenotypes through, respectively, induced (Biesold et al., 2011; Omatsu et al., 2008; Pavlovich et al., 2018) and constitutive (Zhou et al., 2016) expression of type I interferon genes. We verified these published phenotypes on our own cell lines infected with rVSV-G, rVSV-EBOV, and rVSV-MARV via qPCR of IFN-α and IFN-β genes across a longitudinal time series of infection.

Specifically, we carried out multiple time series of infection of each cell line with each of the viruses described above, under mock infection conditions and at MOIs of 0.0001 and 0.001—with the exception of rVSV-MARV on PaKiT01 cell lines, for which infection was only performed at MOI=0.0001 due to limited viral stocks and the extremely low infectivity of this virus on this cell line (thus requiring high viral loads for initial infection). All experiments were run in duplicate on 6-well plates, such that a typical plate for any of the three viruses had two control (mock) wells, two MOI=0.0001 wells and two MOI=0.001 wells, excepting PaKiT01

bioRxiv preprint doi: https://doi.org/10.1101/696195; this version posted July 8, 2019. The copyright holder for this preprint (which was not certified by peer review) is the author/funder, who has granted bioRxiv a license to display the preprint in perpetuity. It is made available under aCC-BY 4.0 International license.

plates, which had two control and four MOI=0.0001 wells at a given time. We justify this PaKiT01 exemption through the expectation that IFN-α expression is constitutive for these cells, and by the assumption that any expression exhibited at the lower MOI should also be present at the higher MOI.

For these gene expression time series, four 6-well plates for each cell line–virus combination were incubated with virus for one hour at 37˚C. Following incubation, virus was aspirated off, and cell monolayers were washed in PBS, then covered with an agar plaque assay overlay to mimic conditions under which infection trials were run. Plates were then harvested sequentially at timepoints of roughly 5, 10, 15, and 20 hours post-infection (exact timing varied as multiple trials were running simultaneously). Upon harvest of each plate, agar overlay was removed, and virus was lysed and RNA extracted from cells using the Zymo Quick RNA Mini Prep kit, according to the manufacturer's instructions and including the step for cellular DNA digestion. Post-extraction, RNA quality was verified via nanodrop, and RNA was converted to cDNA using the Invitrogen Superscript III cDNA synthesis kit, according to the manufacturer's instructions. cDNA was then stored at 4˚C and as a frozen stock at -20˚C to await qPCR.

Prepped cDNA was assayed via qPCR to assess expression of the type I interferon genes, IFN-α and IFN-β, and the housekeeping gene, β-Actin, using primers previously reported in the literature (SI Appendix, Table S2). For qPCR, 2ul of each cDNA sample was incubated with 7ul of deionized water, 1ul of 5UM forward/reverse primer mix and 10ul of iTaq Universal SYBR Green, then cycled on a QuantStudio3 Real-Time PCR machine under the following conditions: initial denaturation at 94˚C for 2 min followed by 40 cycles of: denaturation at 95˚C (5 sec), annealing at 58˚C (15 sec), and extension at 72˚C (10 sec).

bioRxiv preprint doi: https://doi.org/10.1101/696195; this version posted July 8, 2019. The copyright holder for this preprint (which was not certified by peer review) is the author/funder, who has granted bioRxiv a license to display the preprint in perpetuity. It is made available under aCC-BY 4.0 International license.

We report simple δ-Ct values for each run, with raw Ct of the target gene of interest (IFN-α or IFN-β subtracted from raw Ct of the β-Actin housekeeping gene in SI Appendix, Figure S2. Calculation of fold change upon viral infection in comparison to mock using the δ-δ-Ct method (Livak & Schmittgen, 2001) was inappropriate in this case, as we wished to demonstrate constitutive expression of IFN-α in PaKiT01 cells, whereby data from mock cells was identical to that produced from infected cells.

Plaque Assays and Time Series Imaging.

After being grown to ~90% confluency, cells were incubated with pelleted rVSVs expressing eGFP (rVSV-G, rVSV-EBOV, rVSV-MARV). Cell lines were challenged with both a low (0.0001) and high (0.001) multiplicity of infection (MOI) for each virus. In a cell monolayer infected at a given MOI (m), the proportion of cells (P), infected by k viral particles can be described by the Poisson distribution: $P(k) = \frac{e^{-m}m^k}{k!}$, such that the number of initially infected cells in an experiment equals: $1 - e^{-m}$. We assumed that a ~90% confluent culture at each trial's origin was comprised of ~9×10^5 cells and conducted all experiments at MOIs of 0.0001 and 0.001, meaning that we began each trial by introducing virus to, respectively, ~81 or 810 cells, representing the state variable 'E' in our theoretical model. Low MOIs were selected to best approximate the dynamics of mean field infection and limit artifacts of spatial structuring, such as premature epidemic extinction when growing plaques collide with plate walls in cell culture.

Six well plates were prepared with each infection in duplicate or triplicate, such that a control well (no virus) and 2-3 wells each at MOI 0.001 and 0.0001 were incubated simultaneously on the same plate. Cells were incubated with virus for one hour at 37˚C.

bioRxiv preprint doi: https://doi.org/10.1101/696195; this version posted July 8, 2019. The copyright holder for this preprint (which was not certified by peer review) is the author/funder, who has granted bioRxiv a license to display the preprint in perpetuity. It is made available under aCC-BY 4.0 International license.

Following incubation, virus was aspirated off, and cell monolayers were washed in PBS, then covered with a molten viscous overlay (50% 2X MEM/L-glutamine; 5% FBS; 3% HEPES; 42% agarose), cooled for 20 minutes, and re-incubated in their original humidified 37˚C, 5% CO_2 environment.

After application of the overlay, plates were monitored periodically using an inverted fluorescence microscope until the first signs of GFP expression were witnessed (~6-8 hours post-infection, depending on the cell line and virus under investigation). From that time forward, a square subset of the center of each well (comprised of either 64- or 36-subframes and corresponding to roughly 60 and 40% of the entire well space) was imaged periodically, using a CellInsight CX5 High Content Screening (HCS) Platform with a 4X air objective (ThermoFisher, Inc., Waltham, MA). Microscope settings were held standard across all trials, with exposure time fixed at 0.0006 sec for each image. One color channel was imaged, such that images produced show GFP-expressing cells in white and non-GFP-expressing cells in black (Figure 1).

Wells were photographed in rotation, as frequently as possible, from the onset of GFP expression until the time that the majority of cells in the well were surmised to be dead, GFP expression could no longer be detected, or early termination was desired to permit Hoescht staining.

In the case of PaKiT01 cells infected with rVSV-EBOV, where an apparently persistent infection established, the assay was terminated after 200+ hours (8+ days) of continuous observation.

Upon termination of all trials, cells were fixed in formaldehyde (4% for 15 min), incubated with Hoescht stain (0.0005% for 15 min) (ThermoFisher, Inc., Waltham, MA), then imaged at 4X on the CellInsight CX5 High Content Screening (HCS) Platform. The machine was allowed to find

bioRxiv preprint doi: https://doi.org/10.1101/696195; this version posted July 8, 2019. The copyright holder for this preprint (which was not certified by peer review) is the author/funder, who has granted bioRxiv a license to display the preprint in perpetuity. It is made available under aCC-BY 4.0 International license.

optimal focus for each Hoescht stain image. One color channel was permitted such that images produced showed live nuclei in white and dead cells in black. All original and processed images are freely available for download at the following FigShare repository: DOI: 10.6084/m9.figshare.8312807.

Hoestch Staining.

Hoestch stain colors cellular DNA, and viral infection is thought to interfere with the clarity of the stain (Dembowski and DeLuca, 2015). As such, infection termination, cell fixation, and Hoestch staining enables generation of a rough time series of uninfectious live cells (i.e. susceptible + antiviral cells) to complement the images which produced time series of proportion infectious. Due to uncertainty over the exact epidemic state of Hoestch-stained cells (*i.e.* exposed but not yet infectious cells may still stain), we elected to fit our models only to the infectious time series derived from GFP-expressing images and used Hoestch stain images as a posthoc visual check on our fit only (Figure 5, main text, and SI Appendix, Figure S7-8).

Image Processing.

All image processing and data analysis was carried out in R version 3.4 for MacIntosh (R Foundation for Statistical Computing, Vienna, Austria). Original images were imported into R and processed via the package EBImage (Pau, Fuchs, Sklyar, Boutros, & Huber, 2010). Composite images of each well were first split into the 36 or 64-subframes from which they were composed (each subframe represents the visual region of focus for the microscope at the time of imaging). Each subframe was trimmed (to remove border effects), processed individually, and recompiled post-processing into binary form, such that light-colored regions of the original

bioRxiv preprint doi: https://doi.org/10.1101/696195; this version posted July 8, 2019. The copyright holder for this preprint (which was not certified by peer review) is the author/funder, who has granted bioRxiv a license to display the preprint in perpetuity. It is made available under aCC-BY 4.0 International license.

image were assigned a value of 1 (white), and dark regions were assigned a value of 0 (black). In the case of images of GFP-expressing cells, these white regions corresponded to "infectious" cells, while in images of Hoescht-stained nuclei, they indicated live, "uninfected" cells.

Microscope focus was poor for control wells and for subframes early in the time series of each trial before GFP expression became apparent, and the original version of any such subframes were light gray and grainy. Our image processing code identified these subframes as any which possessed a mean pixel value greater than .25 (a value substantially higher than any subframes in which true GFP-expressing or Hoestch-stained cells were visible) and subsequently converted the entire frame to 0 (black).

All other subframes were processed following thresholding methods that have been previously described by the authors of EBImage (Pau et al., 2010). As a first pass, all pixels excepting the top 25% lightest pixels tallied were converted to 0 (black). Next, each image frame was walked through a series of secondary thresholding steps using if-else statements in R, such that the lightness threshold for "infectious" status was elevated in frames which were lighter overall due to manual variation in imaging and focusing. Processed subframes were then reconstructed into composite binary images, which were manually checked against original images to ensure consistent and reliable results.

Post-processing into binary form, the number of discrete shapes with value of 1 were tabulated within each image, using the max(bwlabel(X)) function in EBimage, to determine a cell count per image, again corresponding to a count of infectious cells for GFP-expressing images and to a count of uninfected cells for Hoestch stain images. All image processing and counting scripts, in addition to the resulting data, are freely available for download at the following FigShare repository: DOI: 10.6084/m9.figshare.8312807.

bioRxiv preprint doi: https://doi.org/10.1101/696195; this version posted July 8, 2019. The copyright holder for this preprint (which was not certified by peer review) is the author/funder, who has granted bioRxiv a license to display the preprint in perpetuity. It is made available under aCC-BY 4.0 International license.

Data processing.

GFP-expressing images were processed and cells counted across the duration of each infection trial, thus generating a time series of infectious cells. For a subset of plates, infection was terminated, and cells were fixed, Hoestch stained, and imaged at periodic intervals across the duration of the time series. Processing of these images thus allowed for construction of a corresponding time series of live, uninfected cells. Because of logistical constraints (i.e. many plates of simultaneously running infection trials and only one available imaging microscope), the time course of imaging across the duration of each trial was quite variable. As such, we fitted a series of statistical models to our raw image data to reconstruct reliable values of the infectious proportion of each well per hour for each distinct cell line–virus-MOI combination (18 trials in total; Figure 1; SI Appendix, Figure S1).

There was considerable natural variation in initial cell counts across each trial, resulting from subtle differences in the seeding density and growth duration of time until the trial was initiated when wells were subjectively deemed to have reached “90% confluency.” Baseline cell counts were also different across our three cell lines, which varied substantially in natural size. To correct for this variation, we opted to model the proportion of infectious cell spaces per hour for each well, rather than rely on the raw count data. To this end, we collected the maximum number of live cells counted in susceptible control wells at timepoint 0 and set this count to a rough measure of 100% well occupancy for the cell line in question. Using this method, maximum cell counts were, respectively, 103712, 82308, and 92233 for Vero, RoNi/7.1, and PaKiT01 cell lines, respectively, reflecting innate variation in cell sizes. We then converted all cell counts tabulated via our image processing code across the infectious time trials into

bioRxiv preprint doi: https://doi.org/10.1101/696195; this version posted July 8, 2019. The copyright holder for this preprint (which was not certified by peer review) is the author/funder, who has granted bioRxiv a license to display the preprint in perpetuity. It is made available under aCC-BY 4.0 International license.

proportions by dividing the counts by the total number of possible cell spaces for the cell line in question. Though clearly subject to some error, these methods nonetheless maintained internal consistency in our counting methods and generated reasonable time series. We originally experimented with directly tabulating the proportion of infected versus uninfected space in our binary images; however, this approach impaired our ability to generalize across more or less densely seeded trials, as well as trials on cell lines of disparate sizes. As such, we adopted the count-to-proportion methods described here.

To generate an infectious time series of evenly distributed time steps against which to fit both our mean field and spatial mechanistic models, we next fit a series of statistical models to the proportional data produced from the image processing methods described above. For the GFP-expressing data, we used the mgcv package in R (Wood, 2001) to fit generalized additive models (GAMs) in the Gaussian family, with time elapsed (in hours) post infection as a predictor variable for proportion of infectious cells (the response variable). We fit a separate GAM model to each unique cell – virus – MOI combination, incorporating a random effect of well ID (such that each trial was modeled individually), and we fixed the smoothing parameter at k=7 for all trials, as recommended by the package author (Wood, 2001). The gam.predict() function was used to return a unique estimate of infectious proportions per hour across the duration of the longest running time series for each cell-virus-MOI combination, with random effects averaged across each well.

The uninfected counts from the Hoestch stain data were much less numerous since each count required termination of the infection trial and fixation of cells; by definition, only one data point could be produced per trial. Due to this relative scarcity, we opted to fit a more standard linear regression model, again in the Gaussian family, to these data, rather than using the data-

bioRxiv preprint doi: https://doi.org/10.1101/696195; this version posted July 8, 2019. The copyright holder for this preprint (which was not certified by peer review) is the author/funder, who has granted bioRxiv a license to display the preprint in perpetuity. It is made available under aCC-BY 4.0 International license.

hungry GAM methods employed above. As before, we set time elapsed post infection as the predictor for the Hoestch stain data and produced a unique estimate of the proportion of uninfected cells per hour across the duration of the longest-observed trial. No random effects were included in this model, and the resulting time series were not used in any mechanistic model fitting but were incorporated into plots illustrating natural mortality rates in SI Appendix, Figure S3.

Mean Field Model.

Theoretical Model Details.

To derive the expression for R_0, the basic pathogen reproductive number *in vitro*, we used Next Generation Matrix (NGM) techniques (Diekmann, Heesterbeek, & Metz, 1990; Heffernan, Smith, & Wahl, 2005), employing Wolfram Mathematica (version 11.2) as an analytical tool (SI Appendix, Text S1). R_0 describes the number of new infections generated by an existing infection in a completely susceptible host population; a pathogen will invade a population when $R_0 > 1$. We then analyzed stability properties of the system, exploring dynamics across a range of parameter spaces, using MatCont (version 2.2) (Dhooge, Govaerts, Kuznetsov, Meijer, & Sautois, 2008) for Matlab (version R2018a) (SI Appendix, Table S1).

Theoretical Model Fitting.

The natural mortality rate, μ, and birth rate, b, were selected intentionally to produce sustainable live cell populations over long time scales; they represent the mean of fitted rates we initially explored across the three cell lines (SI Appendix, Figure S3). The incubation rate, σ, and the infection-induced mortality rate, α, were both fixed at $\frac{1}{6}$, an accepted standard for general

bioRxiv preprint doi: https://doi.org/10.1101/696195; this version posted July 8, 2019. The copyright holder for this preprint (which was not certified by peer review) is the author/funder, who has granted bioRxiv a license to display the preprint in perpetuity. It is made available under aCC-BY 4.0 International license.

cellular kinetics (Howat et al., 2006). The rate of antiviral cell regression to susceptible status, c, was fixed at $\frac{1}{144}$, allowing for a 6-day duration of antiviral status.

We estimated cell line–virus-MOI-specific values for β and ρ by fitting the deterministic output of infectious proportions in our mean field model to the statistical mean of each infected cell culture time series (SI Appendix, Figure S5, S6). Fitting was performed by minimizing the sum of squared differences between the deterministic model output and cell line–virus-MOI-specific infectious proportion data at each timestep. We used the differential equation solver lsoda() in the R package deSolve (Soetaert, Petzoldt, & Setzer, 2010) to obtain numerical solutions for the mean field model and carried out minimization using the 'BFGS' algorithm of the optim() function in base R. All model fits were conducted using consistent starting guesses for the parameters, β (β= 3), and where applicable, ρ (ρ = 0.001). In the case of failed fits or indefinite hessians, we generated a series of random guesses around the starting conditions and continued estimation until successful fits were achieved.

All eighteen cell line–virus-MOI combinations of data were fit by an immune absent (ε = ρ = c = 0) version of the theoretical model, and RoNi/7.1 and PaKiT01 data subsets were subsequently fit by induced immunity (ε = 0) and constitutive immunity (ε = 1) versions of the model. Finally, fits were compared across each cell line–virus-MOI combination via Akaike Information Criterion (AIC). All fitting and model comparison script is freely available for download at the following FigShare repository: DOI: 10.6084/m9.figshare.8312807.

Spatial Extensions.

Model Description.

bioRxiv preprint doi: https://doi.org/10.1101/696195; this version posted July 8, 2019. The copyright holder for this preprint (which was not certified by peer review) is the author/funder, who has granted bioRxiv a license to display the preprint in perpetuity. It is made available under aCC-BY 4.0 International license.

Our spatial model was constructed in C++ and implemented in R using the packages Rcpp and RcppArmadillo (Eddelbuettel & Francois, 2011; Eddelbuettel & Sanderson, 2017). Following Nagai and Honda (2001) and Howat et al. (2006), we modeled this system on a two-dimensional hexagonal lattice, using a ten-minute epidemic timestep for cell state transitions. At the initialization of each simulation, we randomly assigned a duration of natural lifespan, incubation period, infectivity period, and time from antiviral to susceptible status to all cells in a theoretical monolayer. Parameter durations were drawn from a normal distribution centered at the inverse of the respective fixed rates of μ, σ, α, and c, as reported with our mean field model. These durations were updated iteratively with each time-step, based on each cell's epidemic status.

Transitions involving the birth rate b, the transmission rate β, and the progression to antiviral rate, ρ, were governed probabilistically and adjusted dynamically based on each cell's local and global environment, with b multiplied by the proportion of susceptible cells within a twelve neighbor radius of a focal dead cell, β multiplied by the proportion of infectious cells within a thirty-six neighbor radius of a focal susceptible cell, and ρ multiplied by the global proportion of exposed and, in the case of PaKiT01 simulations for which $\varepsilon = 1$, also susceptible cells at a given time-step.

Spatial model code is available for public access at the following FigShare repository: DOI: 10.6084/m9.figshare.8312807.

Spatial Model Fitting.

All parameters adopted for spatial modeling exactly replicated those used in mean field models, with the exception of the rate of progression to antiviral status, ρ, for which we explored

bioRxiv preprint doi: https://doi.org/10.1101/696195; this version posted July 8, 2019. The copyright holder for this preprint (which was not certified by peer review) is the author/funder, who has granted bioRxiv a license to display the preprint in perpetuity. It is made available under aCC-BY 4.0 International license.

a range of fixed values, and the transmission rate, β, which we re-estimated for each unique cell-virus combination (spatial models were only fit to data from MOI = 0.001 time sereis). For all cell line–virus combinations, we compared an immune absent version of the model (under which ρ = 0) with four unique alternative values for each cell line–virus combination (excepting Vero cells, for which models were only fit under assumptions of ρ= 0). In the case of RoNi/7.1 and PaKiT01 virus/cell line combinations, we also explored values of: (1) ρ = mean field estimate, (2) ρ = one-tenth of the mean field estimate, (3) ρ = ten times the mean field estimate, and (4) ρ = the upper confidence limit of reported mean field values.

Across all fixed values for ρ for each unique cell-virus combination, we re-estimated the transmission rate, β, by minimizing the sum of squared differences between the infectious proportion output of one run of each spatial stochastic simulation and our statistical time series of infectious proportions. We maximized computational efficiency by fitting a single spatial model simulation on a 1000-cell model approximation of the tissue culture to our data and limited the model's stochasticity during these fit runs by eliminating the distribution for all rate-based parameters (natural lifespan, incubation period, infectivity period, and time to antiviral status), such that all cells were initialized with mean values; nonetheless, the three probabilistic transitions (transmission, birth, and ascendance to antiviral status) remained inherently stochastic. Under these conditions, at MOI=0.001, one exposed cell was introduced at the start of each time series. We originally tested alternative fitting methodologies but found no significant differences in the quality of parameter estimation when minimizing the sum of squared differences between the data and output from a larger cell grid and/or multiple averaged runs of the spatial model.

bioRxiv preprint doi: https://doi.org/10.1101/696195; this version posted July 8, 2019. The copyright holder for this preprint (which was not certified by peer review) is the author/funder, who has granted bioRxiv a license to display the preprint in perpetuity. It is made available under aCC-BY 4.0 International license.

In an effort to avoid local optima, we used simulation techniques to find optimal transmission rates. For each unique model fit, we constructed a matrix of 402 possible values for β, spanning from 0.0001 to 100000, with the most densely distributed range of potential β values clustered most tightly in the range of 0-200. For each β, we ran the stochastic model 45 unique times to generate a matrix of the sum of squared differences between models and data for all 402 possible βs for each of the 33 unique cell line–virus–ρ combinations (a total of 596970 model runs). We fit models to data from three viral time trials across three different cell lines, assuming ρ = 0 always in the case of Vero cells and examining five different possibilities for ρ in the case of RoNi/7.1 and PaKiT01 cell lines. After constructing our matrix of parameter fits across the 45 stochastic replications for each β, we first culled outliers from the replications by removing any model runs which yielded a least squares fit to the data that diverged from the average least squares for that cell line–virus–ρ combination by more than two standard deviations. Once removed, we then took the mean least squared value across the remaining runs, such that we now had a single least squared value for each of the 13266 unique cell line–virus–ρ–β combinations tested. We then obtained the best-fitting value for β for each of the 33 unique cell line–virus–ρ combinations by: (1) culling βs to those which yielded the lowest 5% of mean least squares per cell line–virus–ρ, then (2) further culling that 5% to β values yielding least squares values within three standard deviations of the minimum least squared value recovered, then (3) finally reporting the β value yielding the minimum sum of squares within that data subset, as well as a 95% confidence interval, representing 1.96 standard deviations above and below that value.

Once we had obtained a "best fit" β for each unique cell line–virus–ρ combination, we converted that parameter's least square measure of fit to AIC, based on the number of data points (n) to which each unique cell line–virus combination was fit, assuming that the number of fitted

bioRxiv preprint doi: https://doi.org/10.1101/696195; this version posted July 8, 2019. The copyright holder for this preprint (which was not certified by peer review) is the author/funder, who has granted bioRxiv a license to display the preprint in perpetuity. It is made available under aCC-BY 4.0 International license.

parameters (k) was equal to one (β) under absent immune assumptions and equal to two under induced and constitutive immune assumptions (ρ and β). From these values, we further culled our fit estimates to select the best-fitting ρ - β combination for each unique cell line–virus – immune assumption combination (21 in total). These 21 "best fit" parameter estimates (and the lower and upper confidence limit on each estimate for β) are reported in SI Appendix, Table S4. We originally tested fitting algorithms using optim(), as employed for mean field models but found consistently better fits to the data using the simulation methods outlined here.

Finally, we carried out one last round of model comparison by comparing AIC values across immune assumptions for each unique cell line–virus combination (9 in total). These ultimate best fit combinations are reported in Table 1 and discussed throughout the main text of the manuscript. We used the 21 best fit parameters within each immune assumption to run 10 stochastic model runs visualized in SI Appendix, Figure S9 on scaled-up 10,000 cell grids, as well as a subset of these parameters (those for PaKiT01-rVSVG-EBOV fits only) to run 100,000 cell grids for reporting in Video S1-S3.

All original stochastic model fits and corresponding comparison and figure construction code are available for download at the following FigShare repository: DOI: 10.6084/m9.figshare.8312807.

bioRxiv preprint doi: https://doi.org/10.1101/696195; this version posted July 8, 2019. The copyright holder for this preprint (which was not certified by peer review) is the author/funder, who has granted bioRxiv a license to display the preprint in perpetuity. It is made available under aCC-BY 4.0 International license.

Acknowledgments

CEB was supported by a National Science Foundation Graduate Research Fellowship at Princeton University and a Miller Institute for Basic Research Fellowship at UC Berkeley. Tissue culture experiments were funded by NIH grant R01 AI134824 to KC. Work in LFW's lab was funded by the Singapore National Research Foundation grants (NRF2012NRF-CRP001-056 and NRF2016NRF-NSFC002-013). The authors thank the Chandran lab at Albert Einstein College of Medicine – in particular, Cecilia Harold, Megan Slough, Rohit Jangra, and Tanwee Alkutkar – for technical support during tissue culture experiments. The authors further thank Jessica Metcalf and the Graham lab at Princeton for conceptual guidance throughout the project's development.

bioRxiv preprint doi: https://doi.org/10.1101/696195; this version posted July 8, 2019. The copyright holder for this preprint (which was not certified by peer review) is the author/funder, who has granted bioRxiv a license to display the preprint in perpetuity. It is made available under aCC-BY 4.0 International license.

References

Ahn, M., Anderson, D. E., Zhang, Q., Tan, C. W., Lim, B. L., Luko, K., … Wang, L. F. (2019). Dampened NLRP3-mediated inflammation in bats and implications for a special viral reservoir host. *Nature Microbiology*, *4*, 789–799. https://doi.org/10.1038/s41564-019-0371-3

Arnold, C. E., Guito, J. C., Altamura, L. A., Lovett, S. P., Nagle, E. R., Palacios, G. F., & Sanchez-lockhart, M. (2018). Transcriptomics reveal antiviral gene induction in the Egyptian rousette bat is antagonized in vitro by Marburg virus infection. *Viruses*, *10*(607). https://doi.org/10.3390/v10110607

Baccam, P., Beauchemin, C., Macken, C. A., Hayden, F. G., & Perelson, A. S. (2006). Kinetics of influenza A virus infection in humans. *Journal of Virology*, *80*(15), 7590–7599. https://doi.org/10.1128/JVI.01623-05

Bartlett, M. S. (1957). Measles periodicity and community size. *Journal of the Royal Statistical Society, Series A*, *120*(1), 48–70.

Biesold, S. E., Ritz, D., Gloza-Rausch, F., Wollny, R., Drexler, J. F., Corman, V. M., … Müller, M. A. (2011). Type I interferon reaction to viral infection in interferon-competent, immortalized cell lines from the African fruit bat Eidolon helvum. *PLoS ONE*, *6*(11). https://doi.org/10.1371/journal.pone.0028131

Bonhoeffer, S., May, R. M., Shaw, G. M., & Nowak, M. A. (1997). Virus dynamics and drug therapy. *Proceedings of the National Academy of Sciences*, *94*(13), 6971–6976. https://doi.org/10.1073/pnas.94.13.6971

Brook, C. E., & Dobson, A. P. (2015). Bats as “special” reservoirs for emerging zoonotic pathogens. *Trends in Microbiology*, *23*(3), 172–180.

bioRxiv preprint doi: https://doi.org/10.1101/696195; this version posted July 8, 2019. The copyright holder for this preprint (which was not certified by peer review) is the author/funder, who has granted bioRxiv a license to display the preprint in perpetuity. It is made available under aCC-BY 4.0 International license.

https://doi.org/10.1016/j.tim.2014.12.004

Brook, C. E., Ranaivoson, H. C., Broder, C. C., Cunningham, A. A., Héraud, J.-M., Peel, A. J., … Dobson, A. P. (2019). Disentangling serology to elucidate henipa- and filovirus transmission in Madagascar fruit bats. *Journal of Animal Ecology*, *00*, 1– 16. https://doi.org/10.1111/1365-2656.12985

Calisher, C. H., Childs, J. E., Field, H. E., Holmes, K. V, & Schountz, T. (2006). Bats: Important reservoir hosts of emerging viruses. *Clinical Microbiology Reviews*, *19*(3), 531–545. https://doi.org/10.1128/CMR.00017-06

Coffin, J. M. (1995). HIV population dynamics in vivo: Implications for genetic variation, pathogenesis, and therapy. *Science (New York, N.Y.)*, *267*(5197), 483–489.

Crameri, G., Todd, S., Grimley, S., McEachern, J. A., Marsh, G. A., Smith, C., … Wang, L. F. (2009). Establishment, immortalisation and characterisation of pteropid bat cell lines. *PLoS ONE*, *4*(12), e8266. https://doi.org/10.1371/journal.pone.0008266

Desmyter, J., Melnick, J. L., & Rawls, W. E. (1968). Defectiveness of interferon production and of rubella virus interference in a line of African green monkey kidney cells (Vero). *Journal of Virology*, *2*(10), 955–961. https://doi.org/J. Virol. 1968 2:1955.

Dhooge, A., Govaerts, W., Kuznetsov, Y. A., Meijer, H. G. E., & Sautois, B. (2008). New features of the software MatCont for bifurcation analysis of dynamical systems. *Mathematical and Computer Modelling of Dynamical Systems*, *14*(2), 147–175. https://doi.org/10.1080/13873950701742754

Diekmann, O., Heesterbeek, J. A. P., & Metz, J. A. . (1990). On the definition and computation of the basic reproduction ratio R0 in models for infectious diseases in heterogenous populations. *Journal of Mathematical Biology*, *28*, 365–382.

bioRxiv preprint doi: https://doi.org/10.1101/696195; this version posted July 8, 2019. The copyright holder for this preprint (which was not certified by peer review) is the author/funder, who has granted bioRxiv a license to display the preprint in perpetuity. It is made available under aCC-BY 4.0 International license.

Eddelbuettel, D., & Francois, R. (2011). Rcpp: Seamless R and C++ Integration. *Journal of Statistical Software*, *40*, 1–18. https://doi.org/10.1007/978-1-4614-6868-4

Eddelbuettel, D., & Sanderson, C. (2017). RcppArmadillo: Accelerating R with high-performance C++ linear algebra. *Computational Statistics and Data Analysis*, *71*(2014), 1–16.

Emeny, J. M., & Morgan, M. J. (1979). Regulation of the interferon system: Evidence that Vero cells have a genetic defect in interferon production. *Journal of General Virology*, *43*(1), 247–252. https://doi.org/10.1099/0022-1317-43-1-247

Emery, V. C., Cope, A. V., Bowen, E. F., Gor, D., & Griffiths, P. D. (1999). The dynamics of human cytomegalovirus replication in vivo. *The Journal of Experimental Medicine*, *190*(2), 177–182. https://doi.org/10.1084/jem.190.2.177

Haydon, D. T., Cleaveland, S., Taylor, L. H., & Laurenson, M. K. (2002). Identifying reservoirs of infection: A conceptual and practical challenge. *Emerging Infectious Diseases*, *8*(12), 1468–1473. https://doi.org/10.3201/eid0812.010317

Heffernan, J. M., Smith, R. J., & Wahl, L. M. (2005). Perspectives on the basic reproductive ratio. *Journal of The Royal Society Interface*, *2*(4), 281–293. https://doi.org/10.1098/rsif.2005.0042

Hooper, P., Zaki, S., Daniels, P., & Middleton, D. (2001). Comparative pathology of the diseases caused by Hendra and Nipah viruses. *Microbes and Infection*, *3*(4), 315–322. https://doi.org/10.1016/S1286-4579(01)01385-5

Howat, T. J., Barreca, C., O'Hare, P., Gog, J. R., & Grenfell, B. T. (2006). Modelling dynamics of the type I interferon response to in vitro viral infection. *Journal of the Royal Society, Interface*, *3*(10), 699–709. https://doi.org/10.1098/rsif.2006.0136

bioRxiv preprint doi: https://doi.org/10.1101/696195; this version posted July 8, 2019. The copyright holder for this preprint (which was not certified by peer review) is the author/funder, who has granted bioRxiv a license to display the preprint in perpetuity. It is made available under aCC-BY 4.0 International license.

Kacprzyk, J., Hughes, G. M., Palsson-McDermott, E. M., Quinn, S. R., Puechmaille, S. J., O'Neill, L. A. J., & Teeling, E. C. (2017). A potent anti-inflammatory response in bat macrophages may be linked to extended longevity and viral tolerance. *Acta Chiropterologica*, *19*(2), 219–228. https://doi.org/10.3161/15081109ACC2017.19.2.001

Keeling, M. J., & Rohani, P. (2008). *Modeling infectious diseases in humans and animals.* Princeton, NJ: Princeton University Press.

Kühl, A., Hoffmann, M., Müller, M. A., Munster, V. J., Gnirß, K., Kiene, M., … Pöhlmann, S. (2011). Comparative analysis of Ebola virus glycoprotein interactions with human and bat cells. *Journal of Infectious Diseases*, *204*, S840–S849. https://doi.org/10.1093/infdis/jir306

Kuzmin, I. V., Schwarz, T. M., Ilinykh, P. A., Jordan, I., Ksiazek, T. G., Sachidanandam, R., … Bukreyev, A. (2017). Innate immune response of bat and human cells to filoviruses: Commonalities and distinctions. *Journal of Virology*, *91*(8), e02471-16. https://doi.org/10.1128/JVI.02471-16

Livak, K. J., & Schmittgen, T. D. (2001). Analysis of relative gene expression data using real-time quantitative PCR and the 2^(-ΔΔCT) method. *Methods*, *25*(4), 402–408. https://doi.org/10.1006/meth.2001.1262

Mahanty, S., & Bray, M. (2004). Pathogenesis of filoviral haemorrhagic fevers. *Lancet Infectious Diseases*, *4*(8), 487–498. https://doi.org/10.1016/S1473-3099(04)01103-X

Miller, E. H., Obernosterer, G., Raaben, M., Herbert, A. S., Deffieu, M. S., Krishnan, A., … Chandran, K. (2012). Ebola virus entry requires the host-programmed recognition of an intracellular receptor. *The EMBO Journal*, *31*(8), 1947–1960. https://doi.org/10.1038/emboj.2012.53

Morris, S. E., Yates, A. J., de Stwart, R. L., de Vries, R. D., Mina, M. J., Nelson, A. N., …

bioRxiv preprint doi: https://doi.org/10.1101/696195; this version posted July 8, 2019. The copyright holder for this preprint (which was not certified by peer review) is the author/funder, who has granted bioRxiv a license to display the preprint in perpetuity. It is made available under aCC-BY 4.0 International license.

Grenfell, B. T. (2018). Modeling the measles paradox reveals the importance of cellular immunity in regulating viral clearance. *PLoS Pathogens*, *14*(12), e1007493.

Nagai, T., & Honda, H. (2001). A dynamic cell model for the formation of epithelial tissues. *Philosophical Magazine Part B*, *81*(7), 699–719. https://doi.org/10.1080/13642810108205772

Neumann, A., Lam, N., Dahari, H., Gretch, D., Wiley, T., Layden, T., & Perelson, A. (1998). Hepatitis C viral dynamics in vivo and the antiviral efficacy of Interferon-alpha therapy. *Science (New York, N.Y.)*, *282*, 103–107.

Ng, M., & Chandran, K. (2018). *Unpublished results*.

Ng, M., Ndungo, E., Kaczmarek, M., Herbert, A. S., Binger, T., James, R., … Chandran, K. (2015). NPC1 contributes to species-specific patterns of Ebola virus infection in bats. *ELife*, *4*, e11785. https://doi.org/10.7554/eLife.11785

Nicholls, J. M., Poon, L. L., Lee, K. C., Ng, W. F., Lai, S. T., Leung, C. Y., … Peiris, J. S. (2003). Lung pathogy of fatal severe acute respiratory syndrom. *Lancet*, *361*, 1773–1778. https://doi.org/10.1016/S0140-6736(03)13413-7

Nowak, M. A., Bonhoeffer, S., Hill, A. M., Boehme, R., Thomas, H. C., & McDade, H. (1996). Viral dynamics in hepatitis B virus infection. *Proceedings of the National Academy of Sciences*, *93*, 4398–4402. Retrieved from http://www.pnas.org/content/pnas/93/9/4398.full.pdf

Nowak, M. A., May, R. M., Phillips, R. E., Rowland-Jones, S., Lalloo, D. G., McAdam, S., … McMichael, A. J. (1995). Antigenic oscillations and shifting immunodominance in HIV-1 infections. *Nature*, *375*, 606–611.

Omatsu, T., Bak, E. J., Ishii, Y., Kyuwa, S., Tohya, Y., Akashi, H., & Yoshikawa, Y. (2008).

bioRxiv preprint doi: https://doi.org/10.1101/696195; this version posted July 8, 2019. The copyright holder for this preprint (which was not certified by peer review) is the author/funder, who has granted bioRxiv a license to display the preprint in perpetuity. It is made available under aCC-BY 4.0 International license.

Induction and sequencing of Rousette bat interferon α and β genes. *Veterinary Immunology and Immunopathology*, *124*(1–2), 169–176. https://doi.org/10.1016/j.vetimm.2008.03.004

Pau, G., Fuchs, F., Sklyar, O., Boutros, M., & Huber, W. (2010). EBImage-an R package for image processing with applications to cellular phenotypes. *Bioinformatics*, *26*(7), 979–981. https://doi.org/10.1093/bioinformatics/btq046

Pavlovich, S. S., Lovett, S. P., Koroleva, G., Guito, J. C., Arnold, C. E., Nagle, E. R., … Palacios, G. (2018). The Egyptian Rousette genome reveals unexpected features of bat antiviral immunity. *Cell*, *173*(5), 1098–1110. https://doi.org/10.1016/j.cell.2018.03.070

Pawelek, K. A., Huynh, G. T., Quinlivan, M., Cullinane, A., Rong, L., & Perelson, A. S. (2012). Modeling within-host dynamics of influenza virus infection including immune responses. *PLoS Computational Biology*, *8*(6), e1002588. https://doi.org/10.1371/journal.pcbi.1002588

Peel, A. J., Baker, K. S., Crameri, G., Barr, J. A., Hayman, D. T., Wright, E., … Wood, J. L. N. (2012). Henipavirus neutralising antibodies in an isolated island population of African fruit bats. *PloS One*, *7*(1), e30346. https://doi.org/10.1371/journal.pone.0030346

Peel, A. J., Baker, K. S., Hayman, D. T. S., Broder, C. C., Cunningham, A. A., Fooks, A. R., … Restif, O. (2018). Support for viral persistence in bats from age-specific serology and models of maternal immunity. *Scientific Reports*, *8*(1), 3859. https://doi.org/10.1038/s41598-018-22236-6

Perelson, A S, Neumann, A. U., Markowitz, M., Leonard, J. M., & Ho, D. D. (1996). HIV-1 dynamics in vivo: virion clearance rate, infected cell life-span, and viral generation time. *Science (New York, N.Y.)*, *271*(5255), 1582–1586. https://doi.org/10.1126/science.271.5255.1582

Perelson, Alan S. (2002). Modelling viral and immune system dynamics. *Nature Reviews*

bioRxiv preprint doi: https://doi.org/10.1101/696195; this version posted July 8, 2019. The copyright holder for this preprint (which was not certified by peer review) is the author/funder, who has granted bioRxiv a license to display the preprint in perpetuity. It is made available under aCC-BY 4.0 International license.

Immunology, *2*(1), 28–36. https://doi.org/10.1038/nri700

Plowright, R. K., Peel, A. J., Streicker, D. G., Gilbert, A., McCallum, H., Wood, J., … Restif, O. (2016). Transmission or within-host dynamics driving pulses of zoonotic viruses in reservoir-host populations. *PLoS Neglected Tropical Diseases*, *10*(8), e0004796. https://doi.org/10.1371/journal.pntd.0004796

Rhim, J. S., Schell, K., Creasy, B., & Case, W. (1969). Biological characteristics and viral susceptibility of an African green monkey kidney cell line (Vero). *Proceedings of the Society for Experimental Biology and Medicine*, *132*(2), 670-678.

Saenz, R. A., Quinlivan, M., Elton, D., MacRae, S., Blunden, A. S., Mumford, J. A., … Gog, J. R. (2010). Dynamics of influenza virus infection and pathology. *Journal of Virology*, *84*(8), 3974–3983. https://doi.org/10.1128/JVI.02078-09

Schountz, T. (2014). Immunology of bats and their viruses: Challenges and opportunities. *Viruses*, *6*(12), 4880–4901. https://doi.org/10.3390/v6124880

Soetaert, K., Petzoldt, T., & Setzer, R. W. (2010). Package deSolve: Solving initial value differential equations in R. *Journal Of Statistical Software*, *33*(9), 1–25. https://doi.org/10.18637/jss.v033.i09

Stetson, D. B., & Medzhitov, R. (2006). Type I Interferons in host defense. *Immunity*, *25*(3), 373–381. https://doi.org/10.1016/j.immuni.2006.08.007

Wang, L.-F., & Anderson, D. E. (2019). Viruses in bats and potential spillover to animals and humans. *Current Opinion in Virology*, *34*, 79–89. https://doi.org/10.1016/j.coviro.2018.12.007

Webb, S. D., Keeling, M. J., & Boots, M. (2007). Host-parasite interactions between the local and the mean-field: How and when does spatial population structure matter? *Journal of*

bioRxiv preprint doi: https://doi.org/10.1101/696195; this version posted July 8, 2019. The copyright holder for this preprint (which was not certified by peer review) is the author/funder, who has granted bioRxiv a license to display the preprint in perpetuity. It is made available under aCC-BY 4.0 International license.

Theoretical Biology, *249*(1), 140–152. https://doi.org/10.1016/j.jtbi.2007.06.013

Wong, A. C., Sandesara, R. G., Mulherkar, N., Whelan, S. P., & Chandran, K. (2010). A forward genetic strategy reveals destabilizing mutations in the Ebolavirus glycoprotein that alter its protease dependence during cell entry. *Journal of Virology*, *84*(1), 163–175. https://doi.org/10.1128/JVI.01832-09

Wood, S. N. (2001). mgcv: GAMs and Generalized Ridge Regression for R. *R News*, *1/2*, 20–24.

Xie, J., Li, Y., Shen, X., Xie, J., Li, Y., Shen, X., … Shi, Z. (2018). Dampened STING-dependent interferon activation in bats. *Cell Host and Microbe*, *23*, 297–301.

Zhang, G., Cowled, C., Shi, Z., Huang, Z., Bishop-Lilly, K. a, Fang, X., … Wang, J. (2013). Comparative analysis of bat genomes provides insight into the evolution of flight and immunity. *Science (New York, N.Y.)*, *339*(6118), 456–460. https://doi.org/10.1126/science.1230835

Zhou, P., Tachedjian, M., Wynne, J. W., Boyd, V., Cui, J., Smith, I., … Baker, M. L. (2016). Contraction of the type I IFN locus and unusual constitutive expression of IFN-α in bats. *Proceedings of the National Academy of Sciences*, *113*(10), 2696–2701. https://doi.org/10.1073/pnas.1518240113